NATIONAL UNIVERSITY OF SCIENCE AND TECHNOLOGY
POLITEHNICA BUCHAREST

PhD THESIS – SUMMARY

INTEGRATED APPROACHES TO INVESTIGATING THE MULTIFUNCTIONALITY OF THE MULTICOMPONENT ALLOY Ti-20Zr-5Ta-2Ag

PhD Supervisor:

Prof. Dr. Chem. Ioana DEMETRESCU

Author:

Chem. Radu NARTIȚĂ

SUMMARY

Integrated Approaches to Investigating the Multifunctionality of the Multicomponent Alloy Ti-20Zr-5Ta-2Ag

TABLE OF CONTENTS

SUMMARY

Integrated Approaches to Investigating the Multifunctionality of the Multicomponent Alloy Ti-20Zr-5Ta-2Ag

SUMMARY

Integrated Approaches to Investigating the Multifunctionality of the Multicomponent Alloy Ti-20Zr-5Ta-2Ag

INTRODUCTION

Over the past two decades, the concept of multicomponent alloys designed in equimolar or near-equimolar proportions, known as high-entropy alloys (HEAs), has revolutionized the field of metallic materials. Thanks to their high configurational entropy, these materials exhibit exceptional thermodynamic stability, crystal-lattice distortions that lead to superior hardness, and unexpected synergies among their constituent elements, offering mechanical and functional properties that are difficult to achieve with conventional alloys. At the same time, in biomedical applications, the need for metallic implants with enhanced corrosion resistance, biocompatibility, and antibacterial activity has driven the development of alloys based on combinations of Ti, Nb, Mo, Zr, Hf, Ta, Ag, and Cu.

In this research, the base material chosen was the Ti-20Zr-5Ta-2Ag alloy, developed and patented in 2019 under patent number RO 132031 B1 [1]. This alloy was selected because of the unique synergy between Ti (biocompatibility and mechanical strength), Zr (chemical stability), Ta (corrosion resistance), and Ag (antibacterial activity). The focus of the study is to investigate the multifunctionality conferred on this base material.

The doctoral thesis combines two research directions: on the one hand, the theoretical and experimental foundation of HEAs, with an emphasis on surface treatments and their properties; and on the other, the synthesis and characterization of bioactive coatings applied to the Ti-20Zr-5Ta-2Ag alloy. The overall approach embraces the concept of multifunctionality: the study of the heat-treatment effects on microstructure and electrochemical behavior is geared toward demanding industrial applications—aiming to optimize both corrosion resistance and mechanical durability—while the development and evaluation of bioactive coatings target biomedical performance, specifically biocompatibility and antibacterial efficacy.

The objectives of the thesis are to characterize the microstructure of the Ti-20Zr-5Ta-2Ag alloy after various surface-preparation treatments; to assess the effects of heat treatment on its crystalline structure, chemical composition, and mechanical and electrochemical properties; and to synthesize and characterize a series of bioactive coatings deposited by different techniques, with comparative evaluation of their corrosion resistance and antibacterial activity.

Chapter 1 reviews current trends in high-entropy alloy research, covering the historical evolution of the HEA concept, design strategies for these materials, the classification of major HEA subtypes, and their principal industrial applications.

SUMMARY

Integrated Approaches to Investigating the Multifunctionality of the Multicomponent Alloy Ti-20Zr-5Ta-2Ag

Chapter 2 examines the structure–property relationships in HEAs, analyzing fundamental mechanisms—conFiguretional entropy, lattice distortion, and the "cocktail" effect—and how they correlate with microstructure, mechanical behavior, and electrochemical performance.

Chapter 3 focuses on bioactive coatings, describing preparation methods, essential characterization criteria, and the functional properties they impart to implants.

Chapter 4 presents a comparative study of two surface-preparation treatments for the Ti-20Zr-5Ta-2Ag alloy, emphasizing morphological and chemical surface characterization as well as contact-angle and microhardness measurements.

Chapter 5 investigates the effects of heat treatment on the alloy's structure and properties, detailing the applied conditions, microstructural modifications, phase transformations, and the outcomes of mechanical and electrochemical tests conducted in corrosive environments.

Chapter 6 analyses how bioactive coatings influence corrosion behaviour and antibacterial activity, comparing two deposition techniques, evaluating coating adhesion and surface topography, and reporting corrosion-resistance and antimicrobial-efficacy test results.

Chapter 7 describes, for the first time, the electrochemical deposition of polypyrrole films loaded with naproxen from a natural deep-eutectic solvent onto the Ti-20Zr-5Ta-2Ag alloy, confirming drug incorporation by FT-IR, demonstrating markedly improved hydrophilicity and corrosion resistance, and characterizing sustained naproxen release kinetics.

The final conclusions and outlook section synthesizes the main findings, highlights the original contributions of the thesis, and proposes future research directions to optimize and extend the applicability of the studied materials.

STATE OF DEVELOPMENT AND APPLICATION POTENTIAL OF HIGH-ENTROPY ALLOYS

Chapter 1: Current trends in high-entropy alloy research

High-entropy alloys (HEA) represent a revolution beyond the conventional alloying paradigm, in which one principal element dominates, while the others are added in small proportions for specific improvements [2]–[4]. In 2004, Cantor et al. first reported the formation of equimolar multicomponent alloys, such as $Fe_{166}Cr_{20}Mn_{20}Ni_{20}Co_{20}$, which crystallize in an FCC solid solution through rapid solidification [5]. Subsequently, publications in this field have grown exponentially, exceeding 3,000 articles during 2024.

The strict definition of HEA based on mixing entropy presupposes a random distribution of atoms, but numerous non-equiatomic or dual-phase systems are nevertheless considered HEA on compositional or single-phase solid-solution criteria. In these materials, high entropy confers thermodynamic stability, lattice distortion influences hardness and conductivity, slow diffusion contributes to microstructural stability, and the "cocktail" effect highlights unexpected synergies among elements, leading to exceptional mechanical and catalytic properties [6]–[8].

HEA production includes liquid-state processing, solid-state processing, and additive manufacturing [7]. In particular, additive manufacturing paves the way toward high-entropy refractory alloys (RHEA), with superior mechanical and thermal resistance [9]. Microstructure control is achieved by adjusting cooling rate, composition, and heat treatments, influencing the formation of FCC, BCC, or intermetallic phases [10], [11]. Moreover, severe plastic deformation refines grains and enhances yield strength and hardness, generating ultrafine microstructures for extreme operating conditions [12].In industry, HEAs are being explored for steam turbines, heat exchangers, aerospace, marine, nuclear, cryogenic, and biomedical applications, due to their unique combination of thermal, mechanical, and anticorrosive resistance [13]–[17].

The transition from conventional alloys to multicomponent systems has raised new questions regarding thermodynamic stability, element diffusion, and structural behaviour, and subsequent research has confirmed that HEAs do not exclude classical alloying methods but rather complement them, offering innovative alternatives for advanced metallic materials [18]–[20].

Chapter 2: Structure-property relationships in high entropy alloys

High entropy alloys develop random solid solutions that can be single-phase, with simple crystal structures (FCC, BCC, HCP), or multiphase, such as FCC/BCC combinations or intermetallic $L1_2$/B2. The initial composition, synthesis method and heat treatments govern the nature of the phases and the resulting microstructure [21]–[23]. Grain refinement and chemical homogenization, for example through severe plastic deformation, can transform bicrystalline structures into single-phase nanocrystalline networks, amplifying the strengthening effects of solid solution and Hall–Petch [24]. In parallel, manipulating solidification conditions under ultra-high pressure leads to fine nanoparticle precipitation and controlled phase transformations, enhancing hardness and yield strength [25].

Strengthening mechanisms in HEA combine lattice distortion—caused by variations in atomic sizes and differing moduli—with dislocation accumulation at grain boundaries and thermal effects under high strain rates. In refractory alloys, selecting elements with contrasting shear moduli refines grains and limits atomic diffusion, achieving an optimal balance between strength and ductility without promoting brittle phases [26]. Heat treatments, by tuning annealing temperature and duration, alter the proportion of ordered versus embrittling phases (e.g., $L1_0$ vs. σ), enabling fine adjustment of the strength–ductility trade-off [27].

The mechanical properties of HEA result from the interplay of solid-solution strengthening, mechanical twinning, and work-hardening. Twinning creates additional barriers to dislocation motion, while geometric dislocation accumulation in heterogeneous microstructures sustains strength increases without sacrificing ductility [28]–[30]. At the same time, electrochemical properties depend on microstructure and phase distribution; lamellar stratifications can generate micro-galvanic cells that influence corrosion mechanisms, underscoring the need for optimized post-solidification treatments for high anticorrosive performance [31].

For optimal HEA design, computational methods are essential: CALPHAD predicts phase stability, density functional theory provides insights into electronic structure and formation energies, molecular dynamics explores atomic movements during deformation, and finite-element analysis evaluates mechanical behaviour and substrate–coating interactions. Machine learning complements this toolkit, accelerating the discovery of new compositions and interatomic potentials, thus fully integrating theoretical and experimental data to optimize properties [23], [32], [33].

Chapter 3. Bioactive coatings: preparation, characterization and properties

Surfaces of multiprincipal alloys can be functionalized through various deposition techniques, adapted to each substrate and each molecule of interest. Thermal methods, such as laser cladding after vacuum melting, rapidly densify the film by controlled solidification, while physico-chemical techniques, magnetron sputtering or layer-by-layer additive manufacturing, offer fine tuning of film composition and thickness [34], [35].

Electrodeposition in deep eutectic solvents extends the electrochemical window and allows direct incorporation of bioactive ions and molecules (polymers, antibiotics, peptides) without additional post-treatment steps [36]–[38]. Micro-arc oxidation or anodization form porous oxide layers (TiO_2 nanotubes) with nano-/microporous architectures that favour hydroxyapatite nucleation and osteointegration, while voltage parameters and electrolyte composition control pore size and layer thickness [39]–[42].

Characterization of the coatings combines electrochemical methods to quantify corrosion current and polarization resistance with structural and thermogravimetric analyses and contact-angle measurements for physico-chemical stability [38], [43]–[45]. Mechanical and adhesion properties are evaluated by nano-indentation and scratch tests, and tribo-corrosion "ball-on-disc" assemblies permit simultaneous study of wear and anodic response [46]. Transmission electron microscopy reveals actual layer thickness and nanometric porosity [47], while biological assays (cell viability and adhesion, micro-CT, antimicrobial studies) correlate porous architecture and bioactive composition with osteointegration and bacterial inhibition [48], [49].

The developed coatings combine anticorrosive barrier mechanisms (passivation by stable oxides, dense film formation) with biological functions (controlled release of ions or bioactive molecules, nanotubular structures for osteoconduction). Film formation free energy, electrochemical synergies and mechanical barriers translate into elastic moduli matched to the substrate, increased hardness and resistance to cyclic loading [34].

Integration of therapeutic molecules (antibiotics, antimicrobial peptides, vitamins) into the coating matrix ensures sustained release profiles, biofilm inhibition and osteogenic stimulation, transforming HEA coatings into multifunctional platforms for next-generation implants [50]–[54].

ORIGINAL CONTRIBUTIONS

Chapter 4: Study of surface preparation treatments of the Ti-20Zr-5Ta-2Ag alloy

The study of surface-preparation treatments on the Ti-20Zr-5Ta-2Ag alloy revealed significant changes in topography, chemical composition, surface energy, and mechanical properties depending on the chemical nature of the applied procedure. Scanning electron microscopy (SEM) showed that, in the untreated state, the surface appears relatively smooth due to the native oxide layer (Figure 4.1), whereas the acid-treated (P2) and alkaline-treated (P3) samples display grinding-induced features followed by the topographical modifications from the chemical treatments.

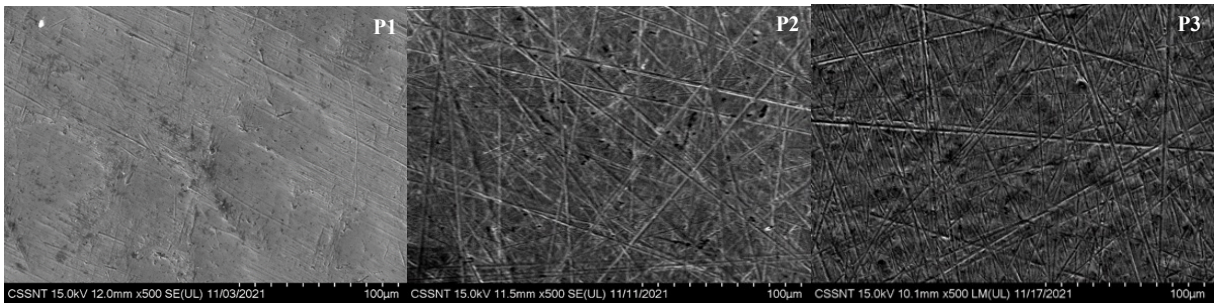

Figure 4.1. SEM images of the Ti-20Zr-5Ta-2Ag alloy surface for untreated (P1), acid treated (P2), and alkaline treated (P3) samples

Atomic force microscopy (AFM) measurements indicated a progressive increase in average roughness Ra from 34 nm (P1) to 58 nm (P2) and 72 nm (P3) (Table 4.1), reflecting a more pronounced relief under NaOH influence.

Table 4.1. Surface-roughness parameters determined by AFM

Parameter	P1 (untreated)	P2 (acid treated)	P3 (alkaline treated)
Ra (nm)	34,03 ± 7,30	58,17 ± 9,93	72,23 ± 11,15
RMS (nm)	44,82 ± 9,48	75,06 ± 12,09	92,43 ± 13,36
Skewness	-0,0576 ± 0,31	-0,4196 ± 0,29	0,2922 ± 0,29
Kurtosis	1,844 ± 0,67	2,456 ± 1,70	1,219 ± 1,73

Energy-dispersive X-ray spectroscopy (EDX) confirmed a homogeneous element distribution on the untreated surface, but composition varied markedly after treatment: the acid

sample showed a decrease in oxygen from 35 at.% to 21 at.% (P2), indicating dissolution of the oxide layer, while the alkaline treatment raised oxygen content to nearly 58 at.% and introduced sodium into the matrix (P3), suggesting formation of sodium titanates and zirconates (Table 4.2).

Table 4.2. Surface chemical composition by EDX for P1, P2, and P3 (in atomic %)

Element	P1 (untreated)	P2 (acid treated)	P3 (alkaline treated)
Ti	55,07 ± 2,42	66,65 ± 1,21	35,65 ± 0,75
Zr	8,36 ± 0,52	9,99 ± 0,32	5,41 ± 0,31
Ta	0,83 ± 0,14	0,93 ± 0,09	0,51 ± 0,09
Ag	0,64 ± 0,14	0,85 ± 0,05	0,50 ± 0,06
O	35,11 ± 2,72	21,59 ± 1,41	57,70 ± 0,74
Na	-	-	0,23 ± 0,07

Physico-chemical properties were evaluated via contact-angle and microhardness measurements: P2 became partially hydrophobic, while P3 became more hydrophilic, consistent with oxide-layer loss and formation of a hydrated titanate layer. Regarding microhardness, the alkaline attack conferred the highest value, exceeding the slightly elevated level of the acid-treated sample (Table 4.3).

Table 4.3. Contact-angle and microhardness values for the analysed samples

Parameter	P1 (untreated)	P2 (acid treated)	P3 (alkaline treated)
Contact angle (°)	81 ± 3.2	100 ± 1.8	56 ± 2.6
Microhardness (HV)	269 ± 7.2	272 ± 4.6	326 ± 5.1

The NaOH reaction mechanism involves partial dissolution of TiO_2 and stepwise formation of $Ti(OH)_4$ species and negatively charged titanates, explaining the observed topographical and chemical transformations [55]–[57]. Thus, for a hydrophilic surface with enhanced mechanical strength and good coating adhesion, alkaline treatment is preferred. For a more reactive surface amenable to further functionalization, a mild acid etch remains an effective option. These results will guide optimization of titanium-based alloy processing for biomedical and industrial applications.

Chapter 5: Effects of heat treatment on the structure and properties of the Ti-20Zr-5Ta-2Ag alloy

After heat treatment, the Ti-20Zr-5Ta-2Ag samples exhibited a visibly altered oxide layer, with colour evolving from light metallic to shades of brown–orange (300 °C), blue (500 °C), and yellow–orange (800 °C), indicative of successive oxide thickening (Figure 5.1) [58]–[60].

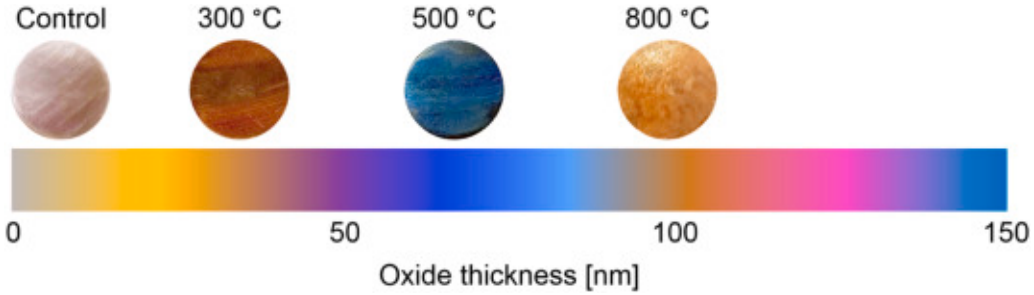

Figure 5.1. Estimated oxide-layer thickness as inferred from sample color changes after heat treatment

SEM micrographs showed that the native oxide layer of only a few nanometres (control) transforms at 300 °C into a thin, still-transparent film over the polishing scratches, while at 500 °C the oxides uniformly cover the surface, and at 800 °C compact oxide particles form and cracks appear, indicating excessive layer embrittlement (Figure 5.2).

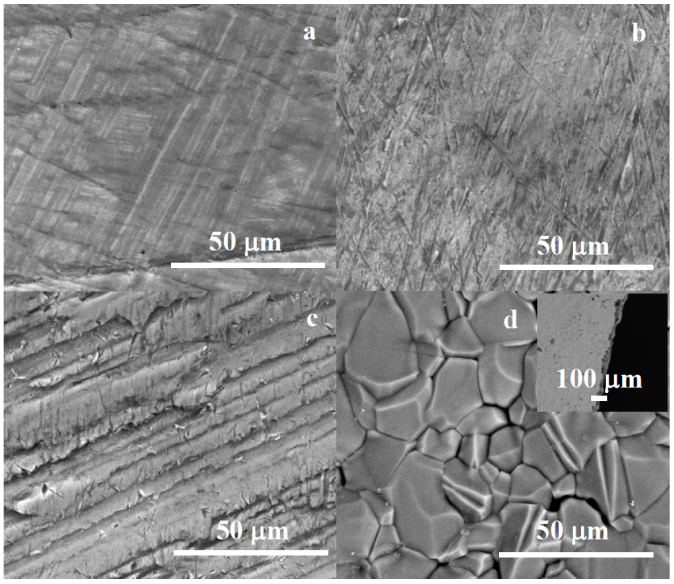

Figure 5.2. SEM micrographs of Ti-20Zr-5Ta-2Ag samples:
(a) control; (b) heat treated at 300 °C; (c) heat treated at 500 °C; (d) heat treated at 800 °C

AFM analysis revealed that the average roughness Ra rises from 56.7 nm (control) to 85.2 nm (300 °C), decreases to 60.7 nm due to oxide alignment in ridges (500 °C), and reaches 363 nm when large oxide crystals dominate the surface (800 °C) (Figure 5.4; Table 5.1).

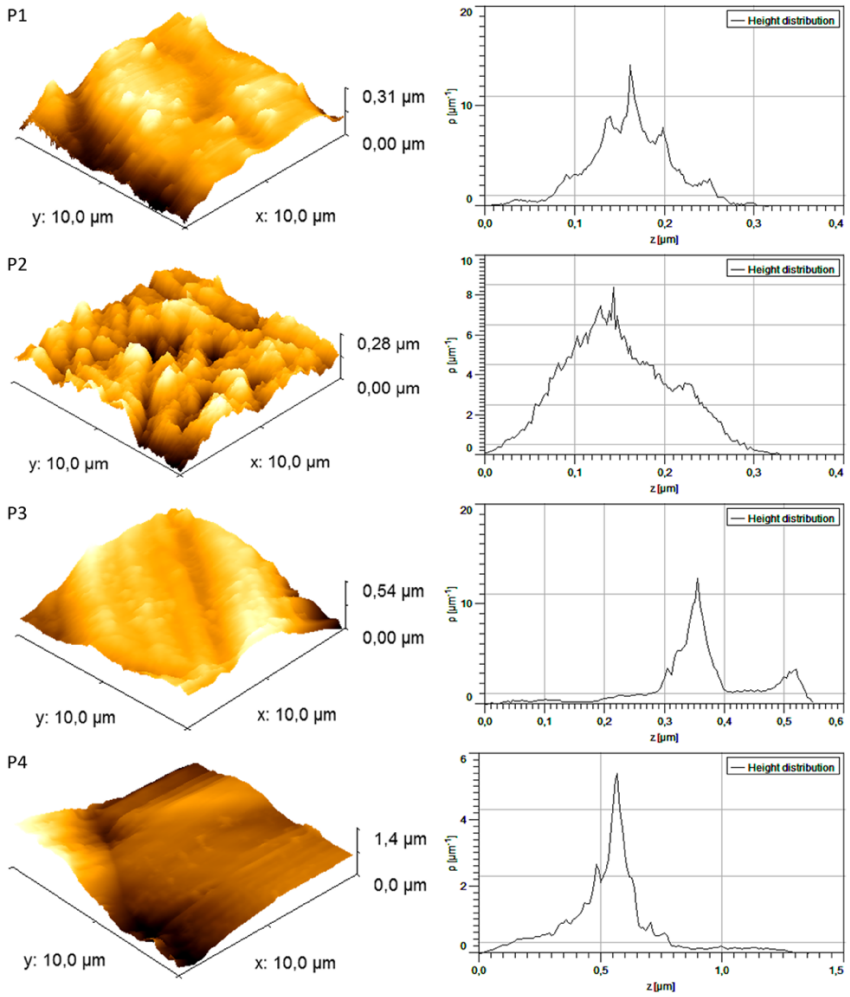

Figure 5.4. AFM topography and roughness analysis of Ti-20Zr-5Ta-2Ag samples: (left) 3D topography images and (right) corresponding height histograms for P1 – control; P2 – 300 °C; P3 – 500 °C; P4 – 800 °C

Table 5.1. TiZrTaAg statistical parameters of surface roughness for Ti-20Zr-5Ta-2Ag samples

Sample	Average roughness [nm]	RMS roughness [nm]	Skewness	Kurtosis
Control	56.7	69.2	-0.454	-0.479
300°C	85.2	105.0	0.045	-0.136
500°C	60.7	87.6	-1.58	4.56
800°C	363	433	-0.212	-0.804

XPS spectroscopy confirmed intensification of the TiO_2, ZrO_2, and Ta_2O_5 peaks up to 500 °C, with silver remaining predominantly metallic and only weak Ag_2O signals; at 800 °C increased noise and mixed-oxide phases reflect a complex oxidation chemistry. XRD revealed that the hexagonal $P6_3/mmc$ structure is retained up to 500 °C, with a slightly contracted unit cell volume and increased crystallite size (14.8 → 22.0 nm), while at 800 °C a partially formed triclinic phase appears, confirming the structural transition (Figures 5.15–5.18; Table 5.2).

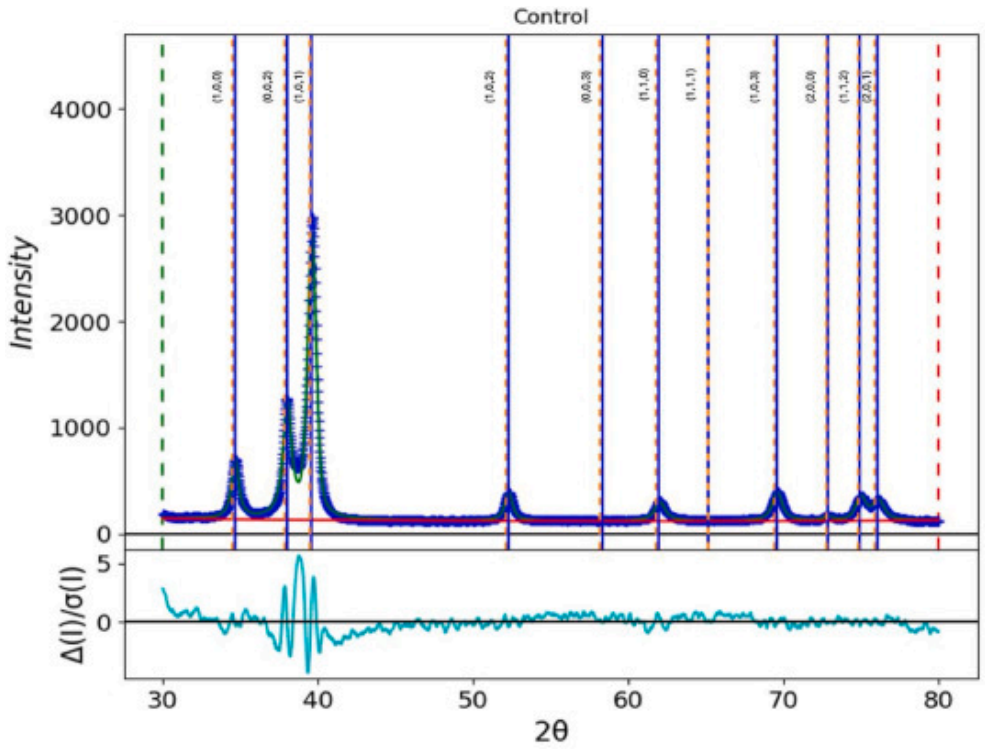

Figure 5.15. XRD model of the control sample (P1). Dashed yellow lines indicate reference positions for the crystal phase; blue lines correspond to experimental peaks. The bottom curve shows the residual difference between experimental data and theoretical model.

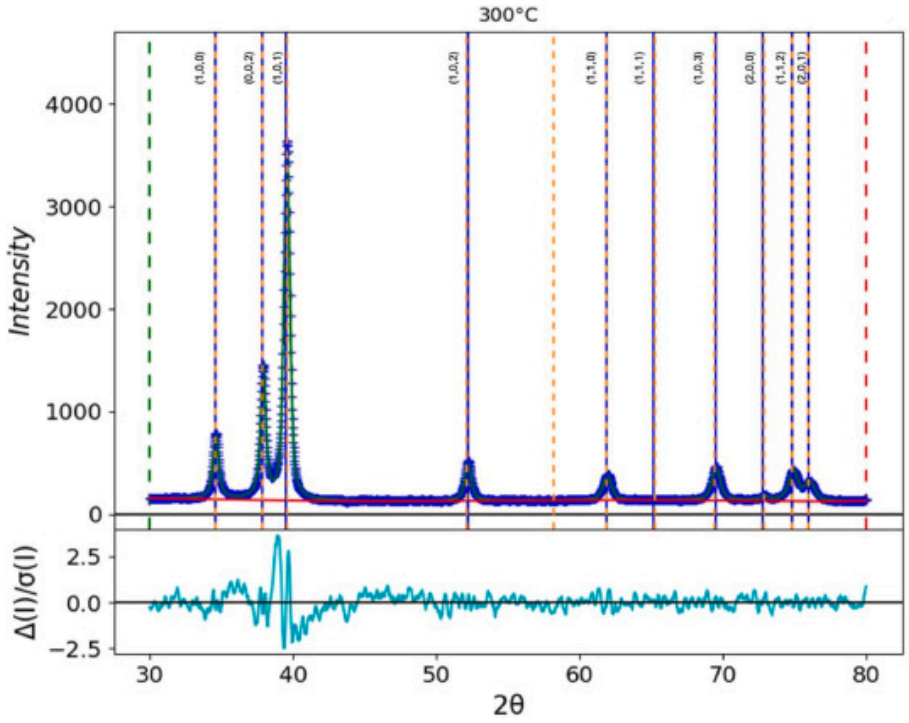

Figure 5.16. XRD model of the sample treated at 300 °C (P2). Dashed yellow lines indicate reference positions for the crystal phase; blue lines correspond to experimental peaks. The bottom curve shows the residual difference between experimental data and theoretical model.

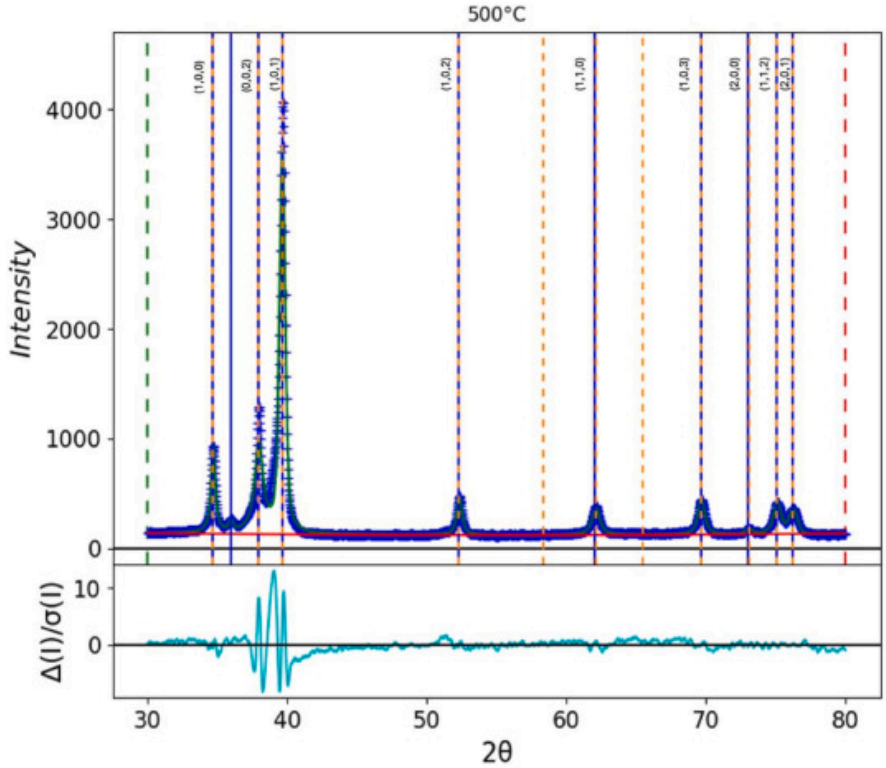

Figure 5.17. XRD model of the sample treated at 500 °C (P2). Dashed yellow lines indicate reference positions for the crystal phase; blue lines correspond to experimental peaks. The bottom curve shows the residual difference between experimental data and theoretical model.

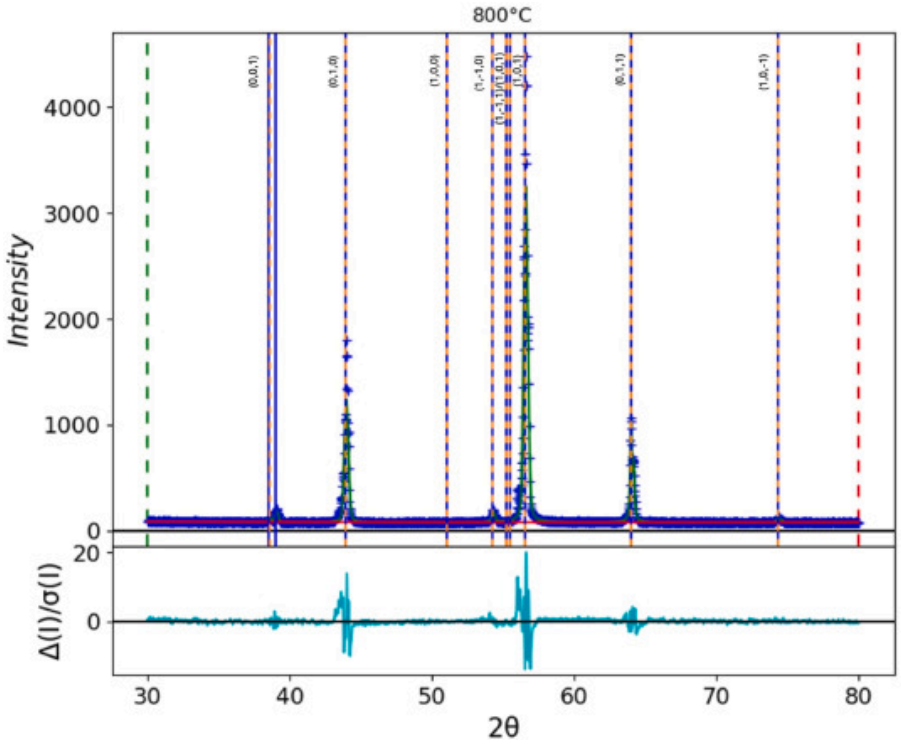

Figure 5.18. XRD model of the sample treated at 800 °C (P2). Dashed yellow lines indicate reference positions for the crystal phase; blue lines correspond to experimental peaks. The bottom curve shows the residual difference between experimental data and theoretical model.

Table 5.2. Unit cell volumes and crystallite sizes of Ti-20Zr-5Ta-2Ag samples

Sample	Unit cell volume (Å³)	Crystallite size (nm)
P1 (control)	37,0	14,8
P2 (300°C)	36,9	18,6
P3 (500°C)	36,6	22,0
P4 (800°C)	9,8	36,2

Vickers microhardness increased from 232 HV (control) to 264 HV (300 °C) and 274 HV (500 °C) due to the ceramic oxide layer; testing at 800 °C was not feasible because of surface degradation.

Electrochemical testing showed that the 300 °C samples exhibited the lowest corrosion current density and highest polarization resistance (0.811 µA/cm², 1090 kΩ·cm²), followed by the 500 °C samples, while corrosion dramatically increased at 800 °C (90 µA/cm², 29 kΩ·cm²)

(Table 5.4; Figure 5.20). EIS spectra confirmed that the 300 °C oxide layer is dense and capacitive (R1 = 328 kΩ; low CPE1), whereas the 800 °C sample required a Warburg element, indicating enhanced diffusion through cracks (Figure 5.21; Table 5.5).

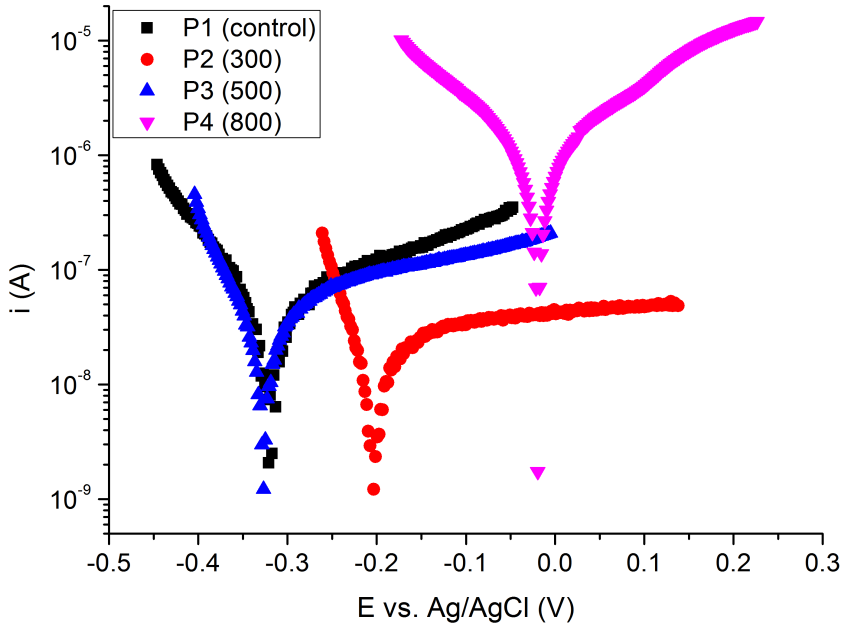

Figure 5.20. Tafel curves for Ti-20Zr-5Ta-2Ag samples

Table 5.4. Corrosion parameters calculated from Tafel curves

Sample	β_a (V dec^{-1})	$\lvert\beta_c\rvert$ (V dec^{-1})	E_{corr} (V)	J_{corr} (A cm^{-2})	Corrosion rate (µm year^{-1})	Polarisation resistance (kΩ cm^2)
P1 (control)	0.13318	0.51393	-0.32079	7.5865E-08	2.8579	605.49
P2 (300°C)	0.06033	0.51766	-0.20529	2.1538E-08	0.8114	1089.50
P3 (500°C)	0.10004	0.52191	-0.32727	5.5656E-08	2.0966	655.08
P4 (800°C)	0.26577	0.40194	-0.01958	2.3989E-06	90.3690	28.96

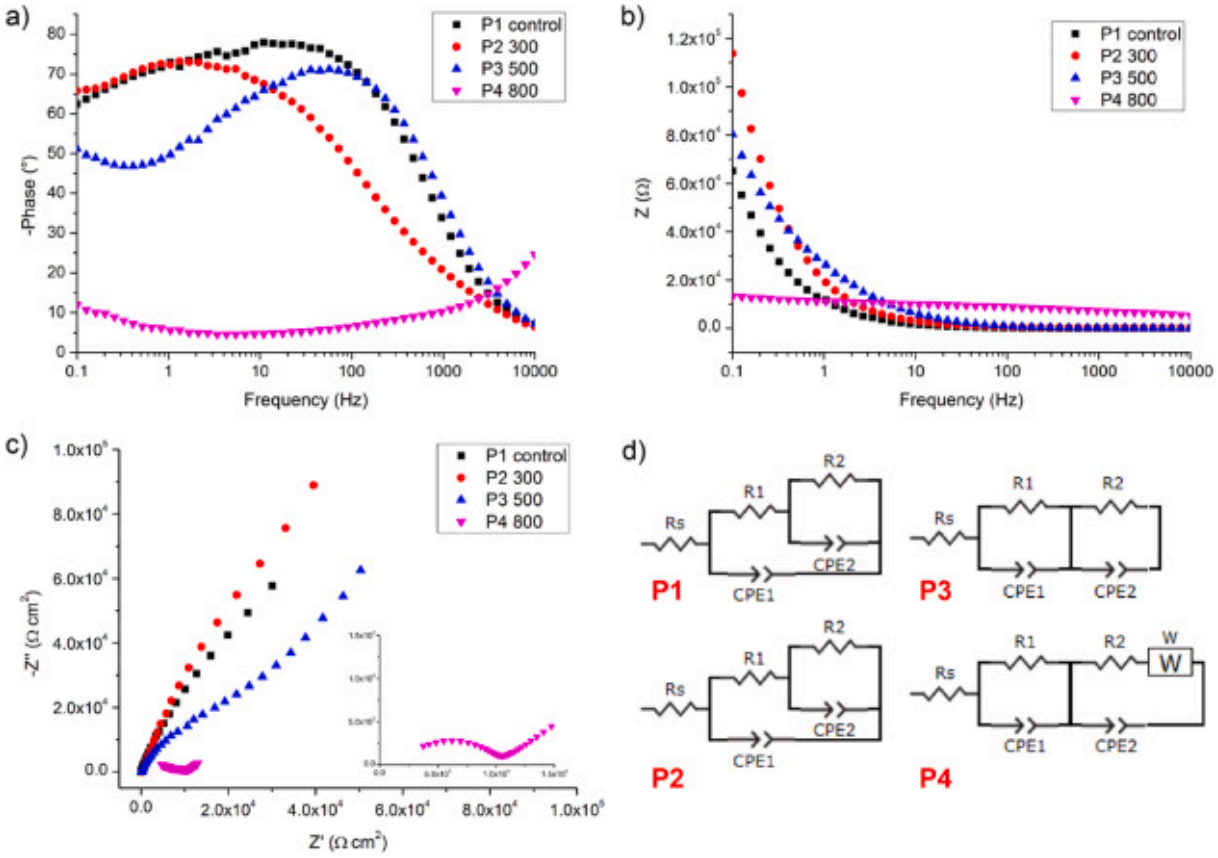

Figure 5.21. EIS results: (a) Bode phase plot, (b) Bode magnitude plot, (c) Nyquist plot detail for P4, and (d) equivalent circuits used to fit the EIS data

Table 5.5. Equivalent-circuit element values obtained from EIS fitting

Sample	Rs (Ω cm²)	R1 (KΩ cm²)	CPE1 (μF cm⁻²)	N1	R2 (KΩ cm²)	CPE2 (μF cm⁻²)	N2	W (μF cm⁻²)
P1 control	35.5	32.8	14.3	0.904	518	9.64	0.648	-
P2 300	209	328	3.71	0.87	699	7.67	0.796	-
P3 500	122	22	6.04	0.858	275	18.3	0.846	-
P4 800	35.5	4.82	1.02	0.835	5.79	6.24	0.416	325

Thus, heat treatments between 300 °C and 500 °C form a uniform oxide layer that enhances hardness, structural stability, and corrosion protection, whereas exposure to 800 °C generates brittle oxides, cracks, and electrochemical degradation—making it advisable to optimize thermal processing below 500 °C for biomedical and industrial applications.

Chapter 6: Influence of different bioactive coatings on the corrosion resistance and antibacterial activity of the Ti-Zr-Ta-Ag alloy

In this chapter, the way two types of bioactive coatings—chitosan–bioglass–ZnO and chitosan–bioglass–GO—deposited either by doctor-blade or by MAPLE, affect the electrochemical stability and antibacterial action of the Ti-20Zr-5Ta-2Ag alloy, was investigated. SEM and EDX analyses showed that, after etching, the bare substrate exhibits irregular grooves and 400–500 nm pores, with local Ag accumulations (Figures 6.1–6.2), whereas the chitosan coating visually smooths the topography and partially masks the substrate signal. Introduction of ceramic ZnO particles (200–300 nm) and bioglass particles (500–2 500 nm) produces a homogeneous surface with discrete agglomerates, suggesting their integration into the polymer matrix.

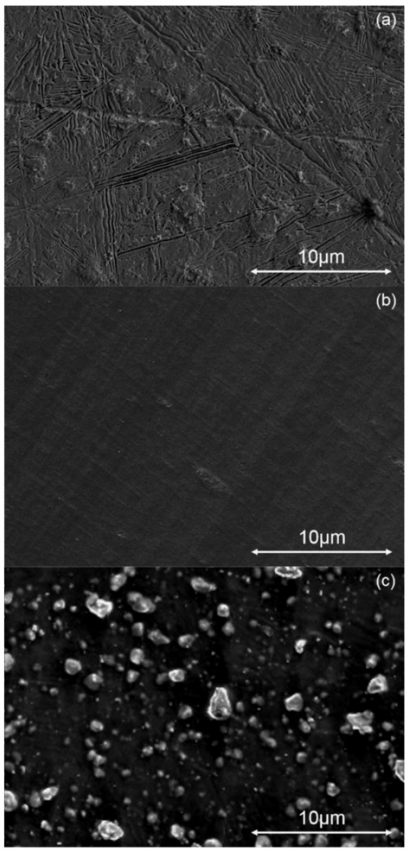

Figure 6.1. SEM micrographs of the samples: (a) bare Ti-Zr-Ta-Ag; (b) Ti-Zr-Ta-Ag + Chitosan; (c) Ti-Zr-Ta-Ag + Chitosan + Bioglass + ZnO

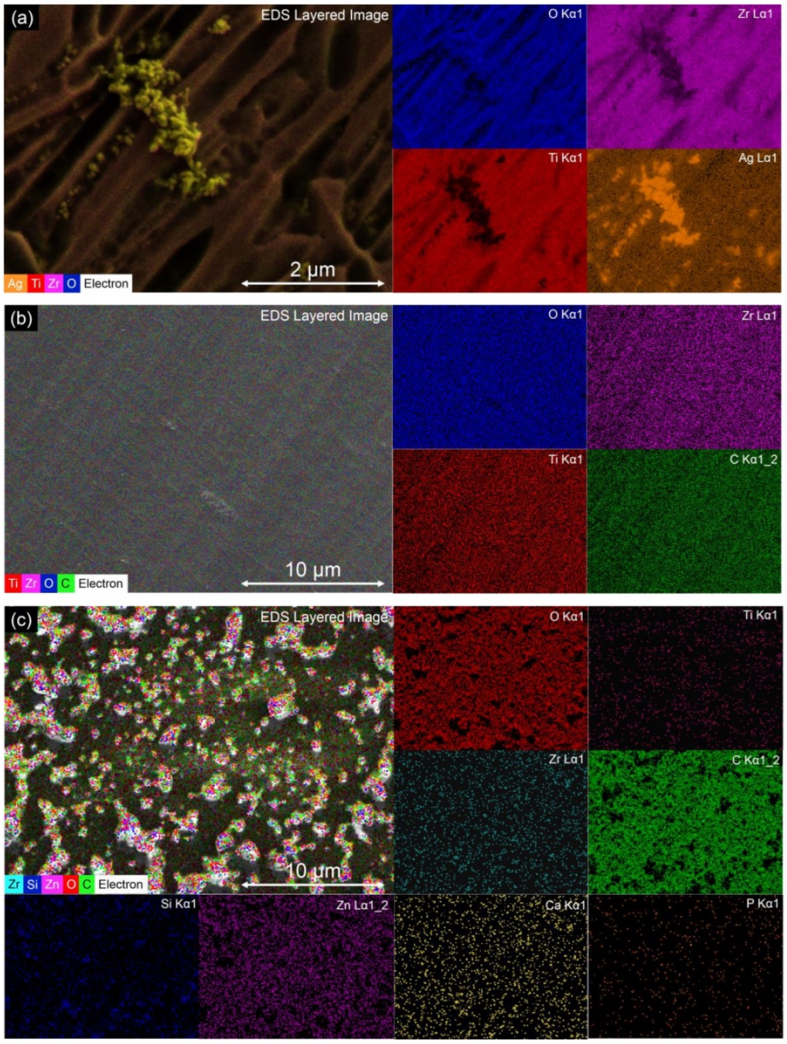

Figure 6.2. EDX maps of the samples: (a) bare TiZrTaAg; (b) TiZrTaAg + Chitosan; (c) TiZrTaAg + Chitosan + Bioglass + ZnO;

When the bare control is immersed in saline, prismatic TiOx and ZrOx structures gradually develop, filling and evening out the polishing grooves after 60 days. The Chi–BG–ZnO film swells progressively, initially releasing ZnO particles and later bioglass fragments, while the Chi–BG–GO film retains its particles fully embedded, showing a rapid initial swelling and stable height histograms after 30 days (Figures 6.3–6.4).

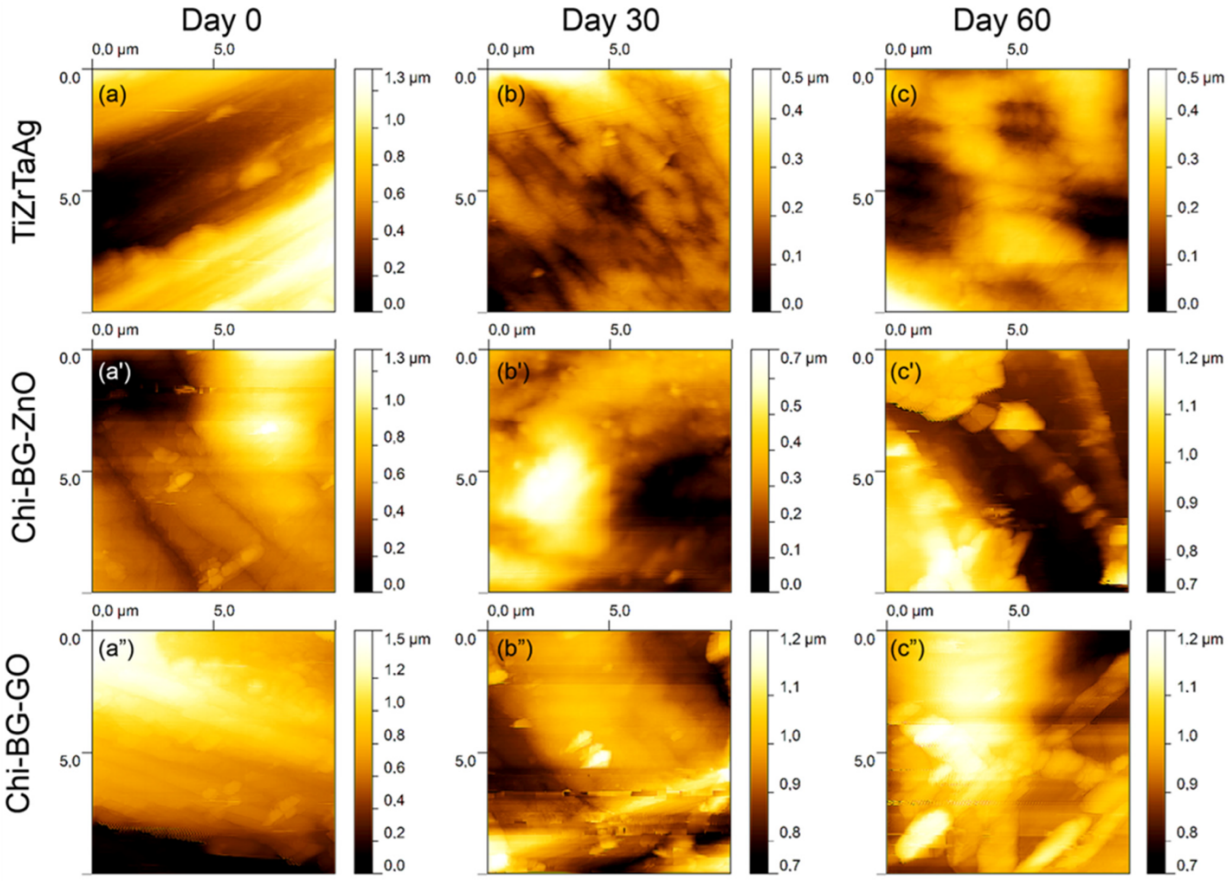

Figure 6.3. AFM microtopographies of the Ti-Zr-Ta-Ag substrate and coated samples at different immersion times: (a) bare substrate before immersion; (a') after 30 days; (a") after 60 days; (b) Chi–BG–ZnO film before immersion; (b') after 30 days; (b") after 60 days; (c) Chi–BG–GO film before immersion; (c') after 30 days; (c") after 60 days.

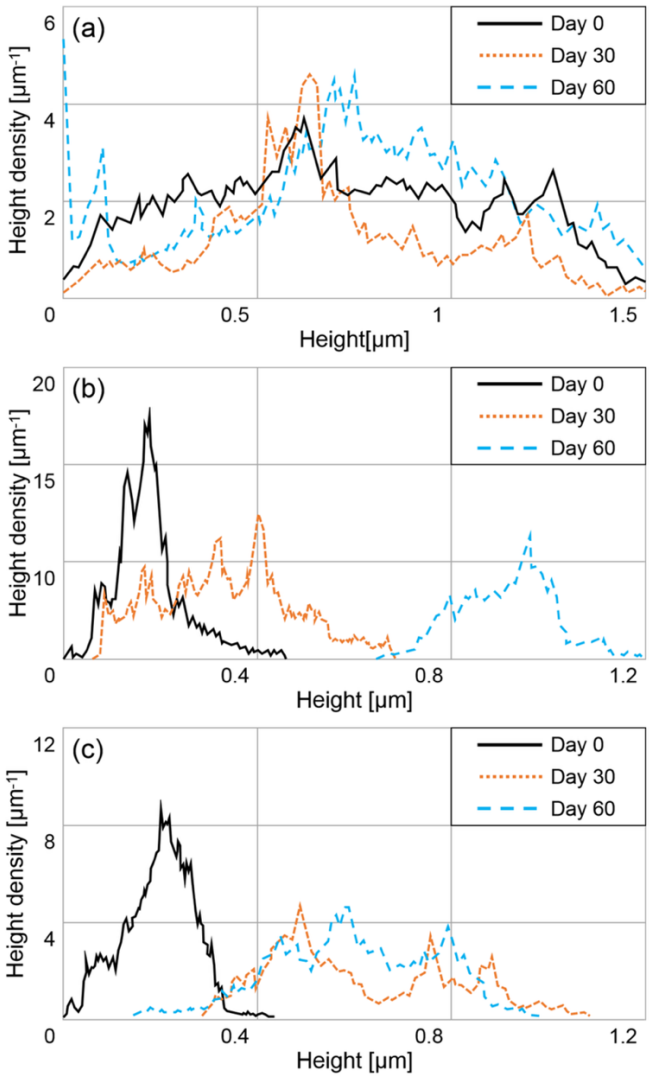

Figure 6.4. Height histograms from AFM after immersion in 0.9 % NaCl for 0, 30, and 60 days: (a) bare substrate; (b) Chi–BG–ZnO film; (c) Chi–BG–GO film.

Average roughness (Ra) decreases from 0.9 µm for the bare alloy to 0.6 µm under chitosan and increases to 1.4 µm under the Chi–BG–ZnO composite (Figure 6.5), whereas for MAPLE-deposited films, Chi–BG–ZnO yields the smoothest surface and Chi–BG–GO undergoes a pronounced roughness increase after 30–60 days (Figure 6.6)

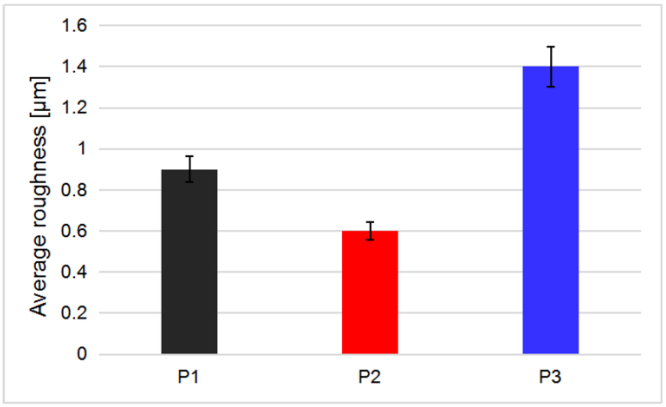

Figure 6.5. Mean Ra values after immersion for: (a) bare TiZrTaAg; (b) TiZrTaAg + Chitosan; (c) TiZrTaAg + Chitosan + Bioglass + ZnO;

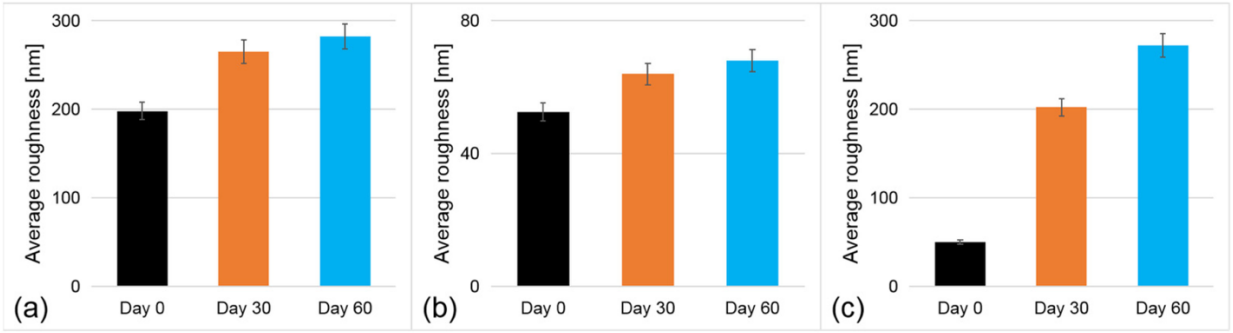

Figure 6.6. Mean Ra values after 0, 30, and 60 days in 0.9 % NaCl for:
(a) bare substrate; (b) film Chi-BG-ZnO, (c) film Chi-BG-GO.

Adhesion evaluations by tip–sample force–distance curves and pull-off tests revealed a maximum adhesion force of 24 nN for the oxidized substrate, reduced to 6 nN under the chitosan film and increased to 16 nN in the presence of ceramic particles (Figure 6.7), while pull-off tests confirm the best adhesion for Chi–BG–ZnO (Figures 6.8–6.9).

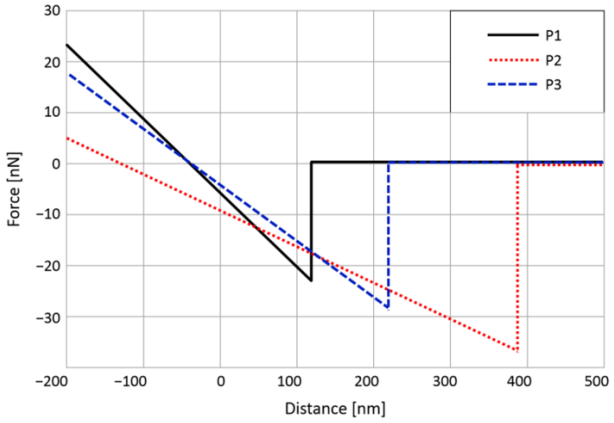

Figure 6.7. AFM F–Z adhesion curves for P1, P2, and P3 by doctor-blade

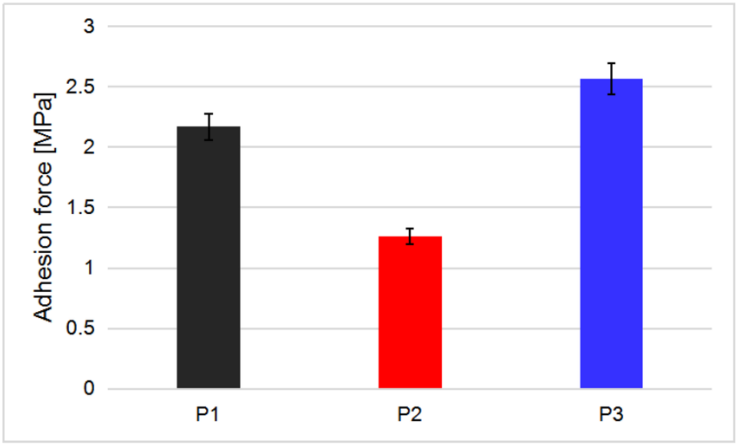

Figure 6.8. Pull-off adhesion forces for doctor-blade coatings.

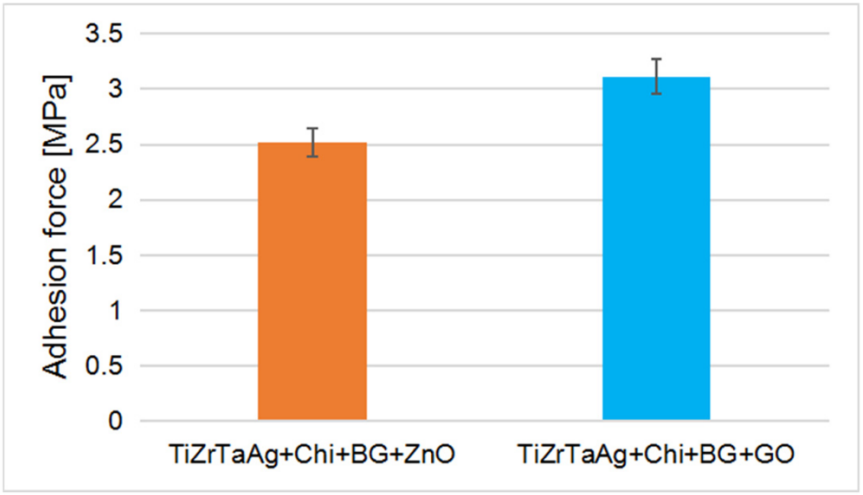

Figure 6.9. Pull-off adhesion forces for MAPLE coatings

Regarding corrosion, Tafel plots for the doctor-blade samples show a significant decrease in current density from the bare alloy to the Chi–BG–ZnO composite, while for MAPLE films, Chi–BG–GO achieves the lowest currents and corrosion rates after 60 days (Table 6.1).

Table 6.1. Corrosion parameters from Tafel curves

Sample	Zi	β_a (V dec^{-1})	$\lvert\beta_c\rvert$ (V dec^{-1})	E_{corr} (V)	J_{corr} (nA cm^{-2})	Corrosion rate (µm $year^{-1}$)
TiZrTaAg – doctor blade	0	0.160	0.134	0.107	355.74	9.76

TiZrTaAg – MAPLE	0	0.169	-0.331	-0.230	24.09	1.94
	30	0.091	-0.258	0.005	17.61	1.26
	60	0.070	-0.218	-0.020	12.09	0.92
TiZrTaAg + Chi+ BG+ ZnO – doctor blade	0	0.405	0.128	-0.108	34.24	0.64
TiZrTaAg + Chi+ BG+ ZnO – MAPLE	0	0.133	-0.071	-0.220	10.33	0.88
	30	0.119	-0.064	0.046	7.40	0.69
	60	0.113	-0.078	-0.060	8.27	0.75
TiZrTaAg + Chi+ BG+ GO – MAPLE	0	0.167	-0.078	-0.293	9.70	0.64
	30	0.067	-0.179	-0.030	4.52	0.38
	60	0.205	-0.056	0.023	7.33	0.42

The best performance was observed for the Chi–BG–GO coating, which exhibited significantly lower corrosion currents and rates compared to all other samples.

EIS plots and equivalent circuits confirm a superior barrier effect for the GO-containing composition, with high R_x and R_f values and low Q_x and Q_h values (Figures 6.12–6.13; Tables 6.2–6.3).

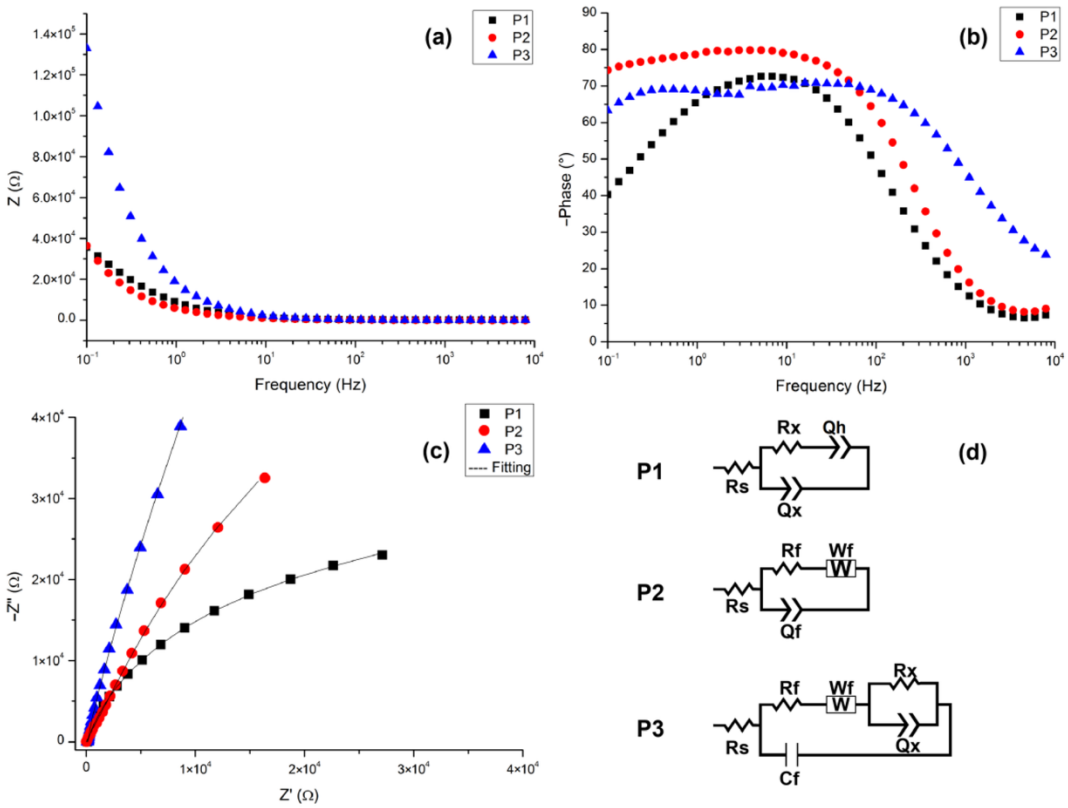

Figure 6.12. EIS Bode (a) magnitude and (b) phase plots; (c) Nyquist plots; (d) equivalent circuits for fitting in 0.9 % NaCl.

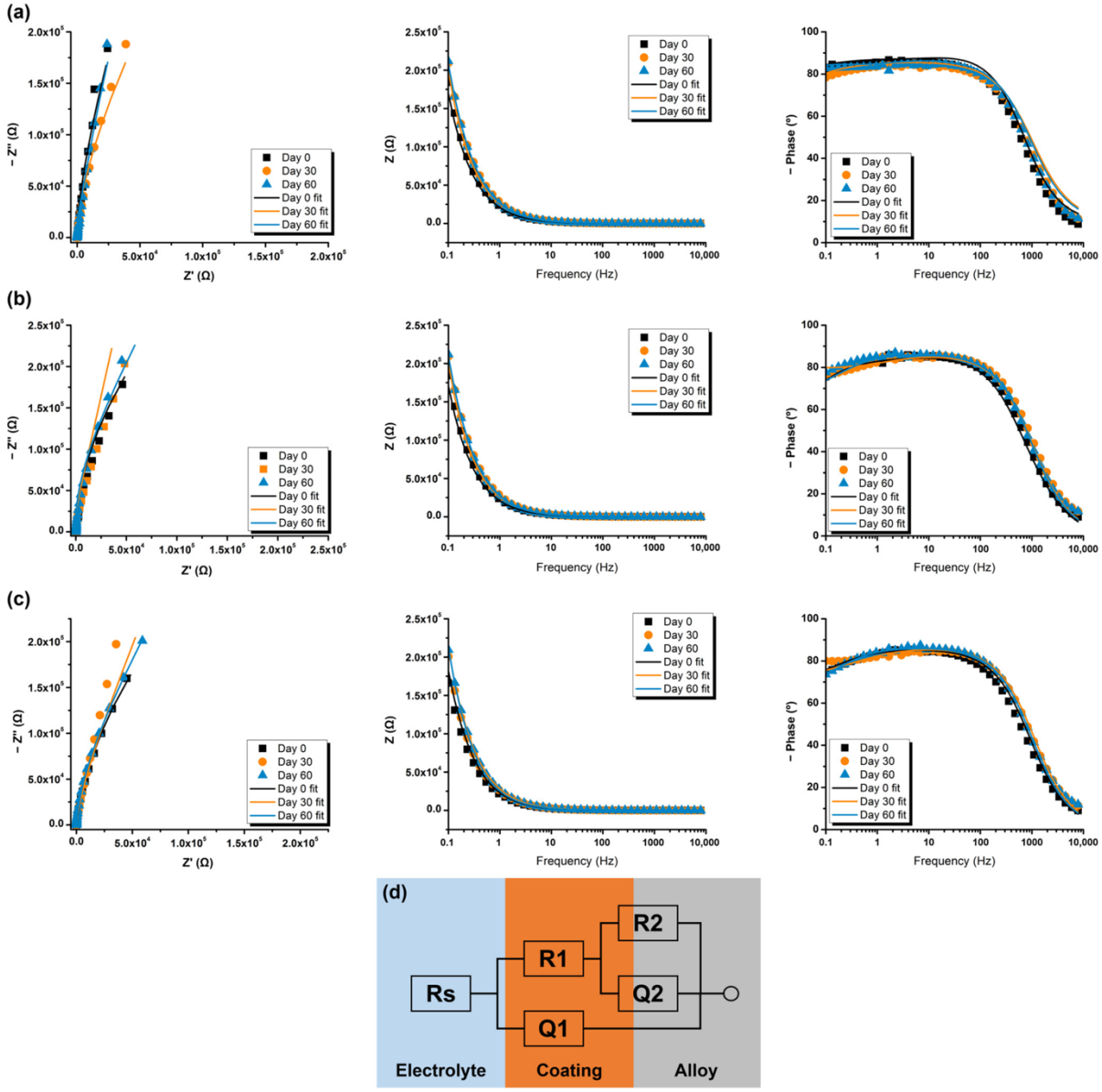

Figure 6.13. Nyquist and Bode plots during 0, 30, and 60 days immersion: (a) bare Ti-Zr-Ta-Ag; (b) Ti-Zr-Ta-Ag + Chi + BG + ZnO; (c) Ti-Zr-Ta-Ag + Chi + BG + GO; (d) equivalent circuits used.

Table 6.2. Equivalent-circuit elements from EIS fitting (doctor blade)

Sample	Rs (Ω cm^2)	Rx × 10^6 (Ω cm^2)	Qx (μF / cm$^2\cdot$s^{n-1})	n_{Qx}	Qh (μF / cm$^2\cdot$s^{n-1})	n_{Qh}	Rf × 10^6 (Ω cm^2)	Qf (μF / cm$^2\cdot$s^{n-1})	n_{Qf}	Cf (μF/cm^2)	Wf (Ω cm^2)	χ^2

TiZrTaAg	109	1.08	21.5	0.84	76.1	0.64	-	-	-	-	-	0.01829
TiZrTaAg + Chitosan	110	-	-	-	-	-	2.3	9.26	0.918	-	2.2	0.03113
TiZrTaAg + Chitosan + BG + ZnO	84	13.1	18.5	0.88	-	-	1.4	-	-	31.7	43.8	0.00909

Table 6.3. Equivalent-circuit elements from EIS fitting (MAPLE)

Sample	Zi	Rs ($\Omega \cdot cm^2$)	R_1 ($k\Omega \cdot cm^2$)	$Q_1 \times 10^{-6}$ ($\Omega^{-1} \cdot s^n \cdot cm^{-2}$)	n_1	R_2 ($k\Omega \cdot cm^2$)	$Q_2 \times 10^{-6}$ ($\Omega^{-1} \cdot s^n \cdot cm^{-2}$)	n_2	X^2
TiZrTaAg	0	33.8	20.7	6.58	0.999	498	22.86	0.924	0.00032
	30	33.0	306	7.60	0.942	787	10.95	0.834	0.00026
	60	32.4	276	7.36	0.957	942	9.12	0.866	0.00041
TiZrTaAg/Chi + BG + ZnO	0	33.5	360	4.92	0.865	1112	15.42	0.884	0.00039
	30	33.6	693	5.49	0.970	2189	10.20	0.916	0.00027
	60	33.5	489	6.70	0.962	1810	12.96	0.958	0.00035
TiZrTaAg/Chi + BG + GO	0	36.8	468	3.41	0.999	6123	8.36	0.855	0.00029
	30	34.5	721	4.12	0.959	9864	3.66	0.724	0.00012
	60	33.9	840	5.31	0.964	3585	6.38	0.778	0.00016

ICP-MS showed that, while the bare substrate releases only trace Ti, the Chi–BG–ZnO film progressively delivers Si (up to ~90 ppm), Ca, P, and Zn, whereas Chi–BG–GO partially retains release, with Si ≈ 90 ppm at 60 days and a slower Zn release rate (Figure 6.14).

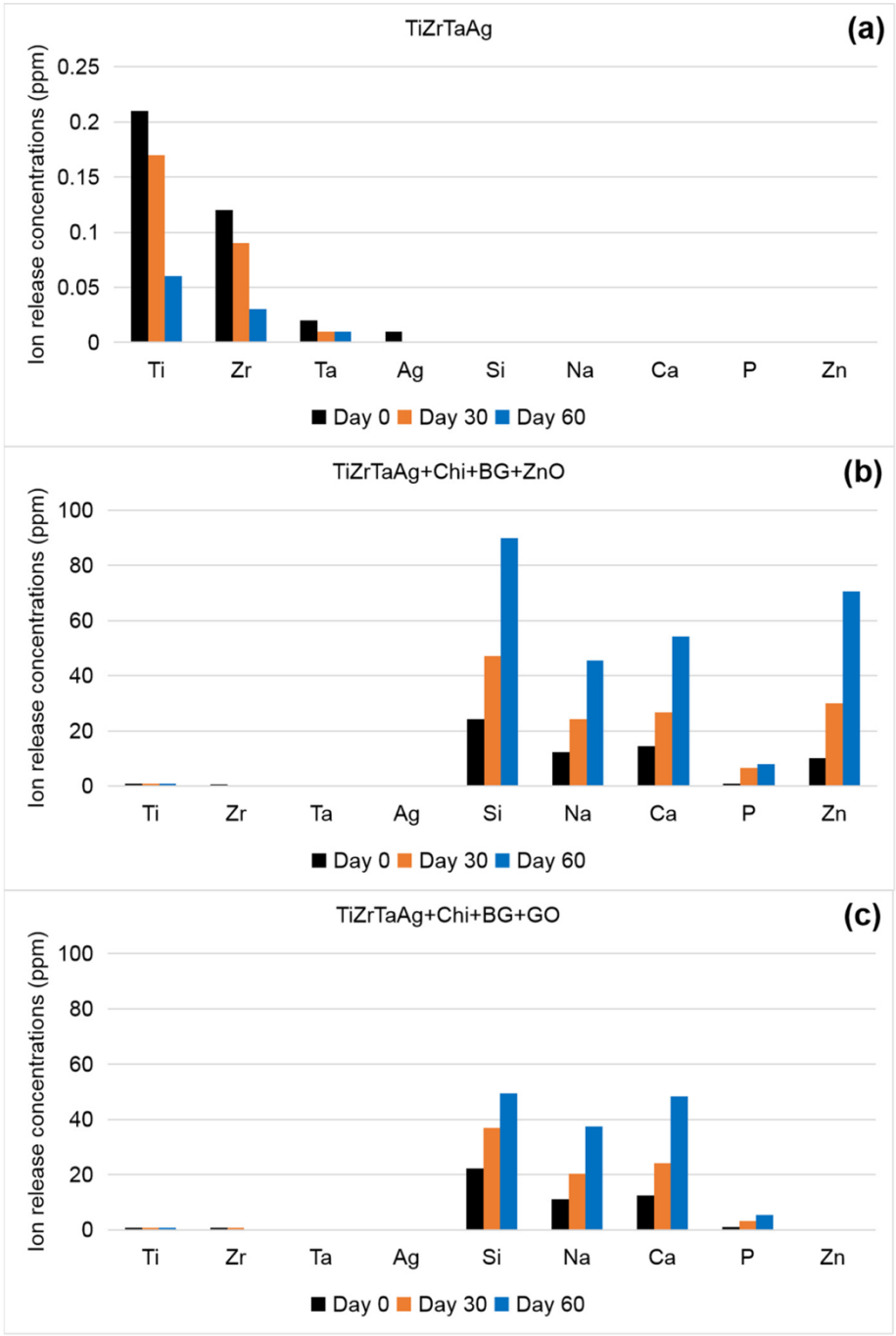

Figure 6.14. Ion-release profiles over 60 days in 0.9 % NaCl for: (a) TiZrTaAg; (b) TiZrTaAg + Chi + BG + ZnO; (c) TiZrTaAg + Chi + BG + GO.

In antibacterial assays against *E. coli* and *S. aureus*, all coatings reduce OD_{600} in the first 48 hours, but Chi–BG–GO shows the strongest inhibition—up to 83 % for *S. aureus* and 71 % for *E. coli*—supported by the largest inhibition-zone diameters (Figures 6.15–6.17).

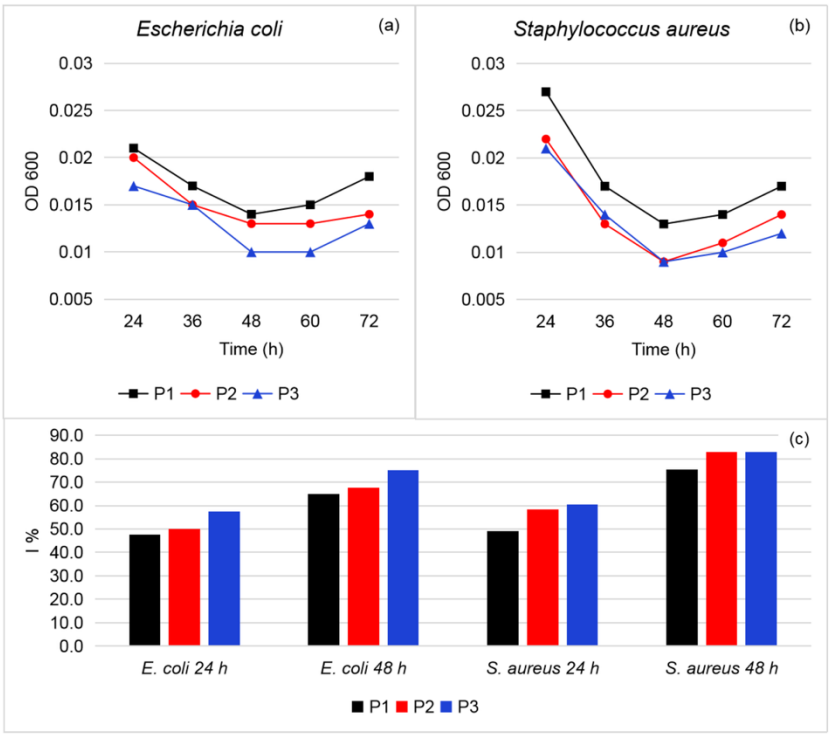

Figure 6.15. Antibacterial activity against (a) *E. coli* and (b) *S. aureus*; (c) Bacterial-growth-inhibition index

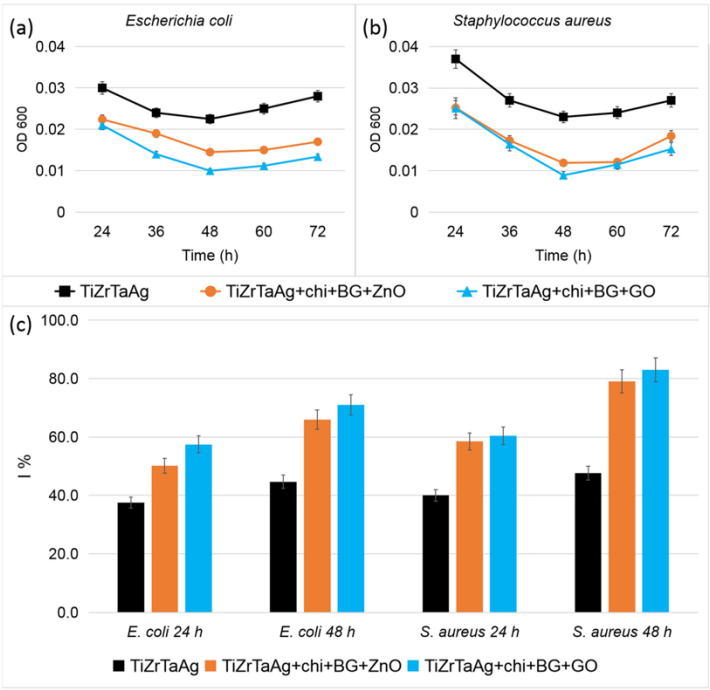

Figure 6.16. Antibacterial activity against (a) *E. coli* and (b) *S. aureus*; (c) Bacterial-growth-inhibition index

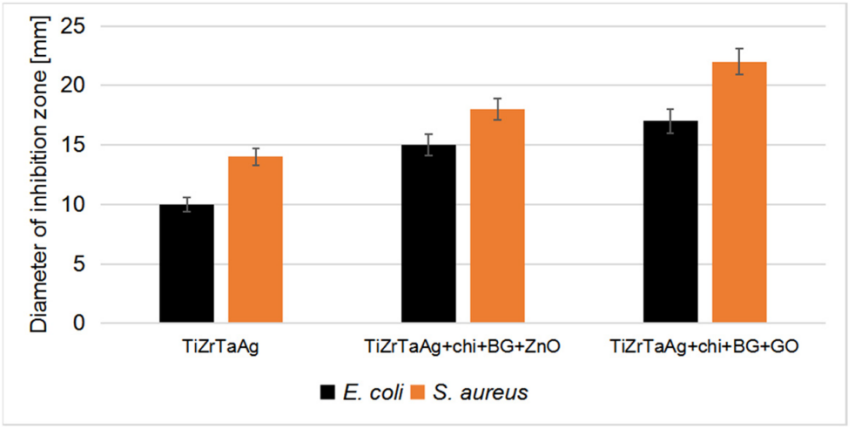

Figure 6.17. Inhibition-zone diameters after 24 hours

Overall, comparison of the two deposition techniques confirms that the Chi–BG–GO film offers the best compromise between anticorrosive protection, mechanical strength of the layer, and antimicrobial activity, via a compact structure, controlled ion release, and GO's "contact killing" mechanism (Figure 6.18) [61], [62].

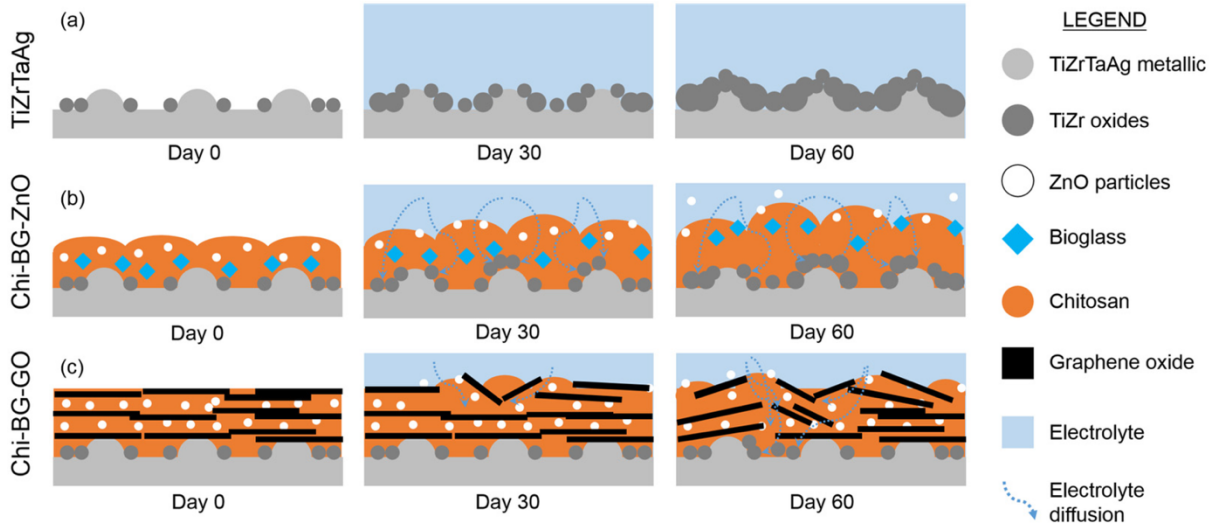

Figure 6.18. Proposed mechanism for film evolution during immersion:
(a) bare Ti-Zr-Ta-Ag; (b) TiZrTaAg + Chi + BG + ZnO; (c) TiZrTaAg + Chi + BG + GO.

Chapter 7: Simultaneous electrodeposition of polypyrrole–naproxen from a natural deep eutectic solvent (NADES) onto the Ti-20Zr-5Ta-2Ag alloy

Chapter 7 describes the electrochemical synthesis of polypyrrole films loaded with Naproxen (PPy–NAP) directly from a natural deep eutectic solvent (NADES) onto the Ti-20Zr-5Ta-2Ag alloy and their morphological, electrochemical and pharmacokinetic characterization. Cyclic voltammograms revealed clear anodic and cathodic peaks associated with pyrrole oxidation and polymer reduction, intensified in the presence of Naproxen (Figures 7.1–7.2).

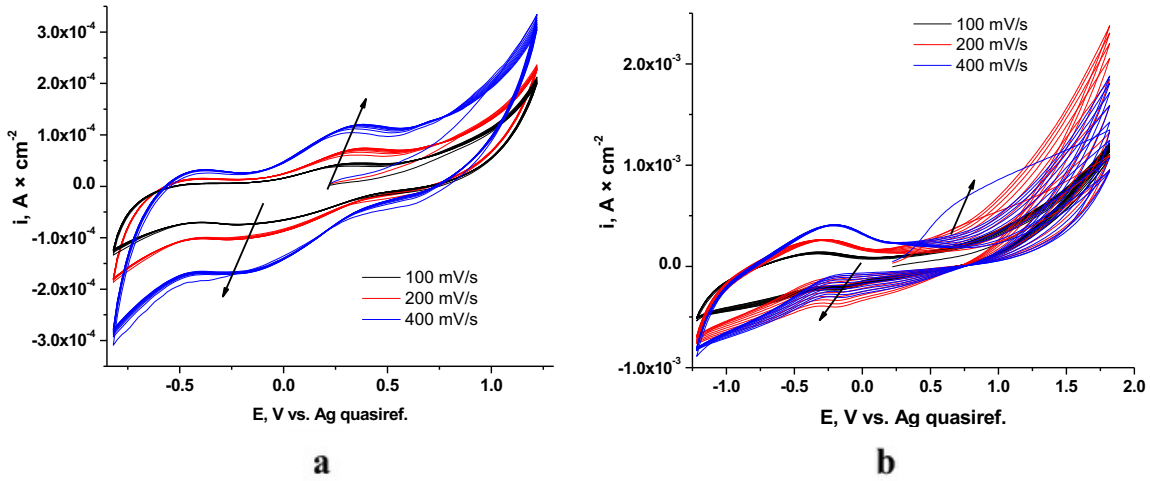

Figure 7.1. Cyclic voltammograms of electrodeposition on Ti–Zr–Ta–Ag alloys recorded at different scan rates for (a) PPy and (b) PPy+NAP

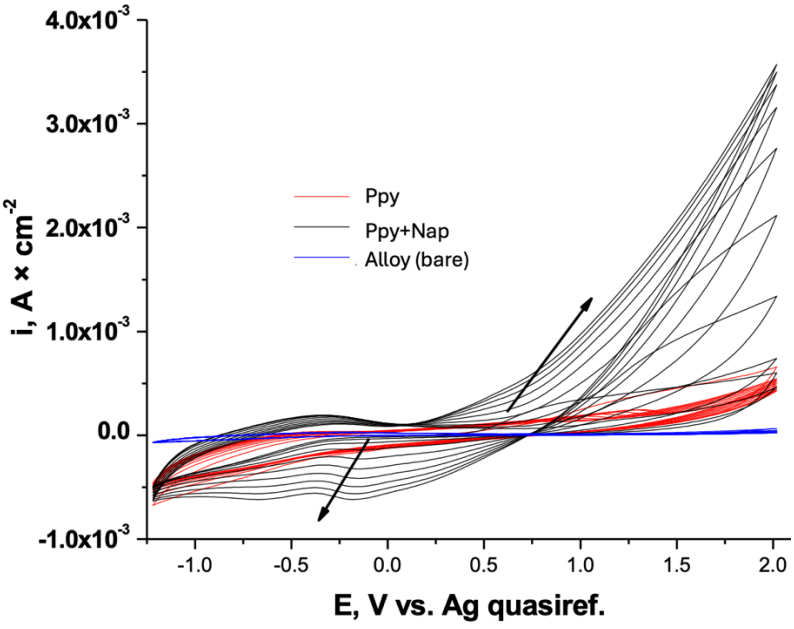

Figure 7.2. Comparative cyclic voltammograms recorded for Ti–Zr–Ta–Ag in monomer-free electrolyte, with pyrrole monomer, and with pyrrole + Naproxen, at 200 mV·s^{-1}

Electropolymerization of pyrrole on Ti-20Zr-5Ta-2Ag was carried out simultaneously by chronoamperometry and chronopotentiometry to obtain both neat PPy and PPy loaded with Naproxen. In potentiostatic mode, the I–t curves showed a sharp current spike at initiation—most pronounced at 1.6 V—followed by a gradual decay due to mass-transport limitations; Naproxen amplified the peak current densities, suggesting accelerated charge transfer. In galvanostatic mode, the potential reached a steady level at 1 mA faster and at higher values than at 0.5 mA, indicating formation of thicker films and conductivity changes induced by drug incorporation. Q–t plots showed a proportional increase of charge with applied potential or current, demonstrating the ability to tune film thickness by deposition parameters (Figures 7.3–7.4).

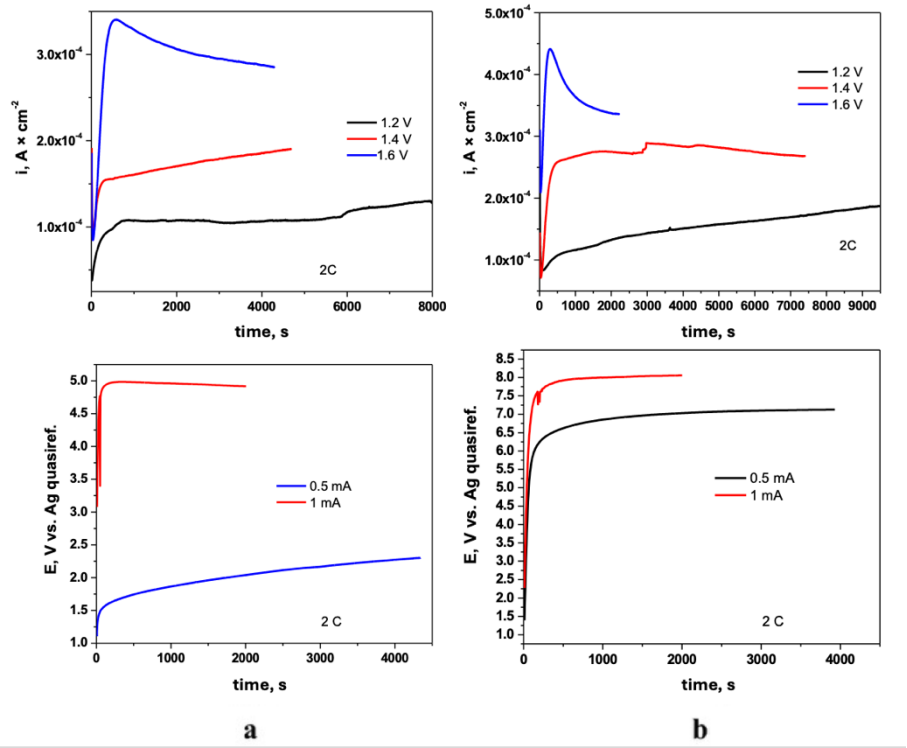

Figure 7.3. Chronoamperometric and chronopotentiometric profiles for PPy (a) and PPy–NAP (b) electrodeposition on Ti-20Zr-5Ta-2Ag in NADES

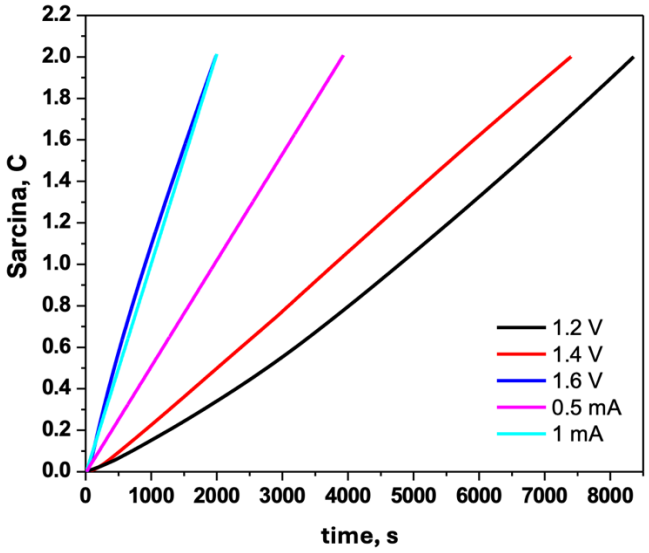

Figure 7.4. Comparative charge–time (Q–t) plots for PPy+NAP films deposited potentiostatically (1.2 V, 1.4 V, 1.6 V) and galvanostatically (0.5 mA, 1 mA)

Optical and SEM micrographs showed that neat PPy uniformly covers the substrate, while Naproxen incorporation alters polymer nucleation into a sponge-like nodular network (potentiostatic deposition) or a denser, more compact film (galvanostatic deposition) (Figure 7.5).

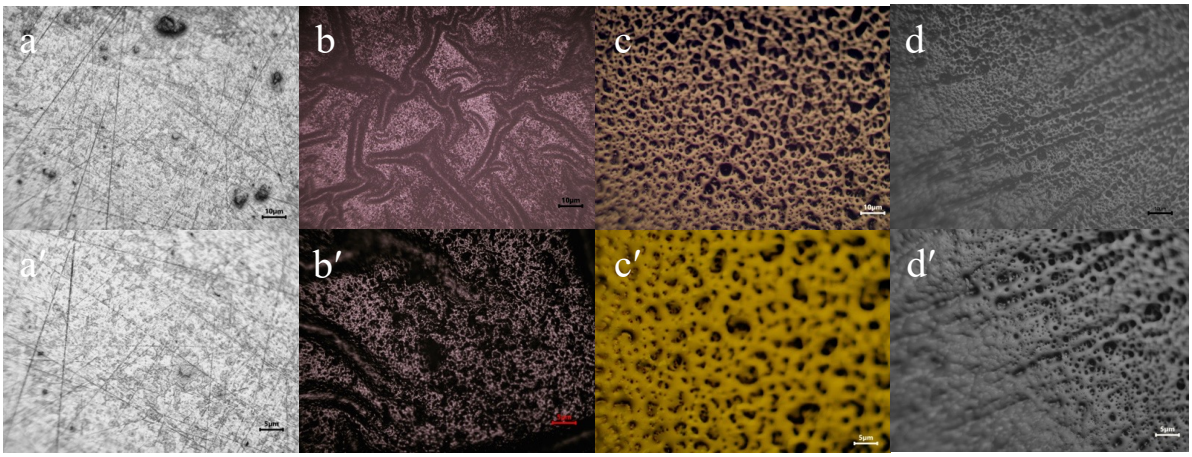

Figure 7.5. Optical micrographs of bare Ti-20Zr-5Ta-2Ag and after coating: a, a′ – bare alloy; b, b′ – PPy; c, c′ – PPy+NAP (potentiostatic); d, d′ – PPy+NAP (galvanostatic); a–d: 10×, scale bar 10 μm; a′–d′: 20×, scale bar 5 μm.

Overlaid FT-IR spectra confirm the presence of polypyrrole bands (N–H, C=C, C–N) and Naproxen signals (aromatic C–H, COO^-, C–O–C), demonstrating chemical integration of the drug into the matrix (Figure 7.7).

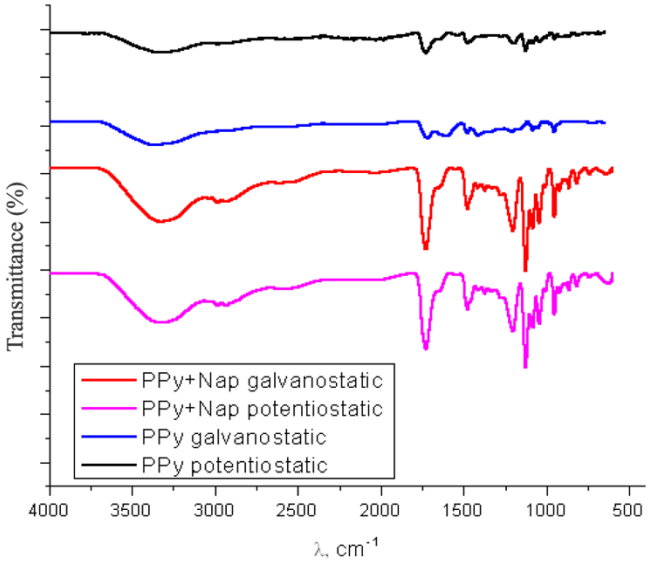

Figure 7.7. Overlaid FT-IR spectra (4000–600 cm^{-1}) for Ti-20Zr-5Ta-2Ag+PPy and Ti-20Zr-5Ta-2Ag+PPy–NAP coatings

Contact-angle measurements show a transition from 31° (bare alloy) to 11–13° under PPy and to 4–10° under PPy–NAP, creating a superhydrophilic surface favorable for protein adsorption and cell proliferation (Figure 7.8).

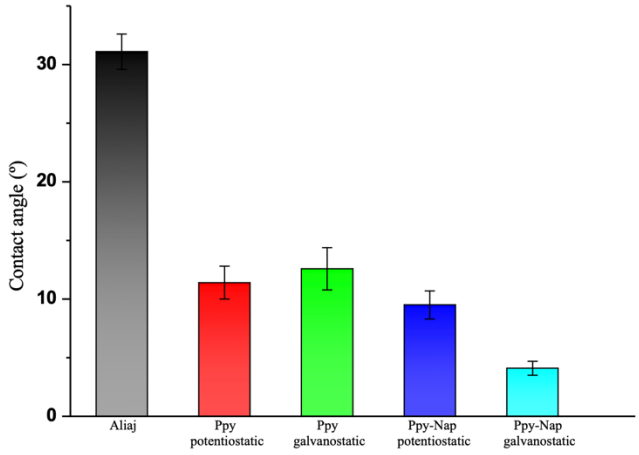

Figure 7.8. Static contact-angle measurements (mean ± SD, n = 5) for bare Ti-20Zr-5Ta-2Ag and coated with PPy or PPy–NAP (potentiostatic and galvanostatic)

In simulated body fluid (SBF), open-circuit potentials of PPy and PPy–NAP films stabilize in ~20 min and shift positively relative to the bare alloy, indicating an effective electrochemical barrier. Tafel plots show that for PPy, corrosion current density drops from ~754 $\mu A \cdot cm^{-2}$ (bare alloy) to 6.8 $\mu A \cdot cm^{-2}$ (potentiostatic, 1.6 V, 2 C) and 4.5 $\mu A \cdot cm^{-2}$

(galvanostatic, 1 mA, 2 C), while for PPy–NAP, i_o ranges between 1.26 and 5.52 $\mu A \cdot cm^{-2}$ depending on deposition conditions. Corrosion potential (Ecorr) shifts positively and polarization resistance (Rp) increases from 0.063 $k\Omega \cdot cm^2$ (bare) to 5.9–11.2 $k\Omega \cdot cm^2$ (PPy) and 9.8–37.8 $k\Omega \cdot cm^2$ (PPy–NAP), confirming the films as very effective corrosion barriers.

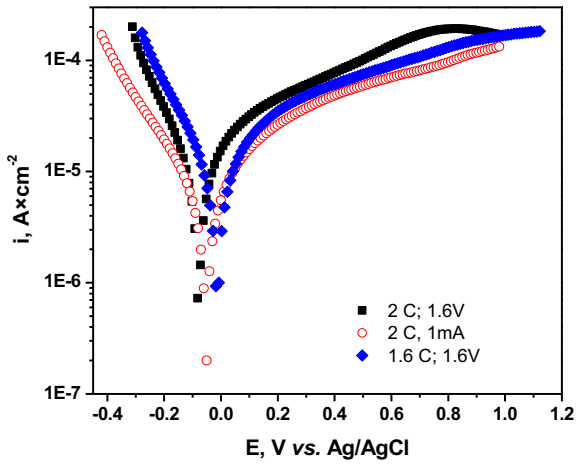

Figure 7.11. Potentiodynamic polarization curves in SBF for PPy coatings deposited potentiostatically at 1.6 V (2 C and 1.6 C) and galvanostatically at 1 mA (2 C)

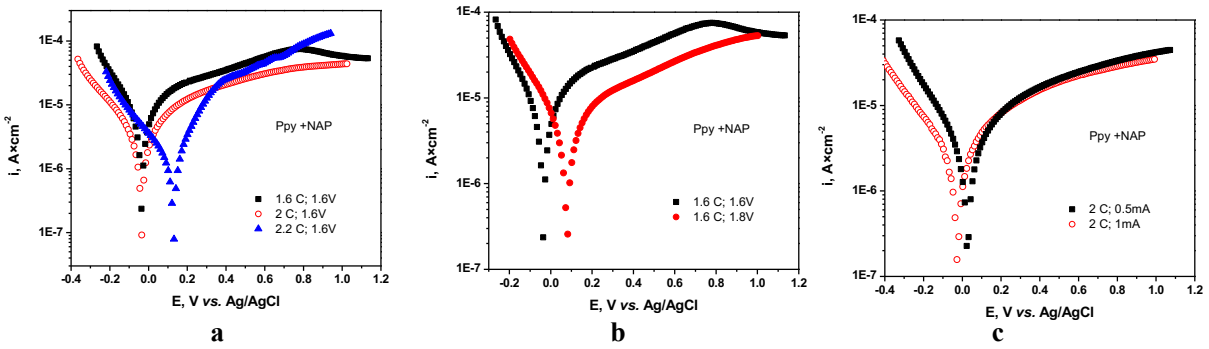

Figure 7.12. Potentiodynamic polarization curves in SBF for PPy–NAP coatings deposited potentiostatically at 1.6 V (1.6 C, 2 C, 2.2 C), 1.8 V (1.6 C) and galvanostatically at 0.5 mA and 1 mA (2 C)

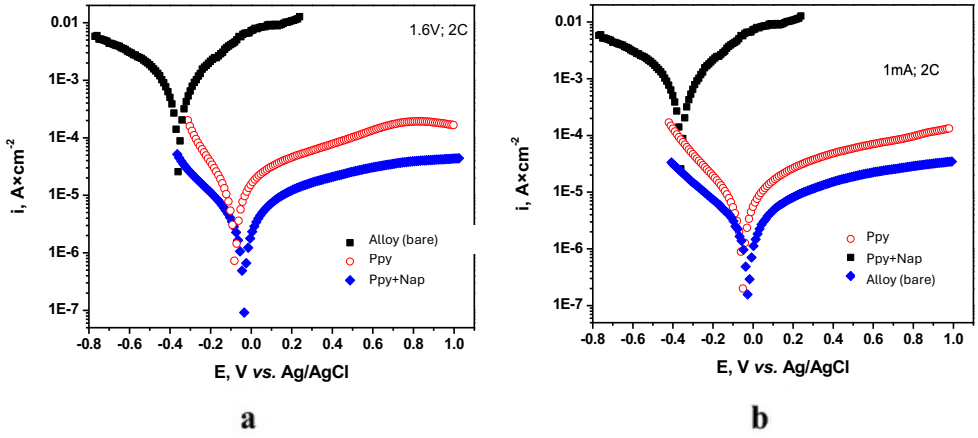

Figure 7.13. Comparative Tafel plots (Q = 2 C) in SBF for bare alloy, PPy-coated and PPy–NAP-coated: (a) potentiostatic (1.6 V, 2 C); (b) galvanostatic (1 mA, 2 C)

Table 7.1. Polarization parameters for Ti-20Zr-5Ta-2Ag coated with PPy and PPy + Naproxen

Material		Tafel slope extrapolation				Polarization resistance		Pi (%)	P (%)
	Deposition conditions	E_{corr}, mV	i_{corr}, μA × cm^{-2}	Kg, g × m^2× h^{-1}	V_{corr}, mm × year^{-1}	R_p, kΩ × cm^2	i_{corr}, μA × cm^{-2}		
Alloy (bare)		−373 ± 0.5	754 ± 1.2	10.65 ± 0.3	14.22 ± 0.1	0.063 ± 0.02	722 ± 1.5	-	-
PPy/Alloy	2C; 1.6V	−69 ± 0.3	6.81 ± 0.02	0.096 ± 0.005	0.128 ± 0.03	6.80 ± 0.7	6.04 ± 0.05	99.09 ± 0.01	3.85 × 10^{-4} ± 0.03
	2C; 1mA	−59 ± 0.3	4.5 ± 0.04	0.064 ± 0.002	0.085 ± 0.001	11.15 ± 0.5	4.21 ± 0.01	99.40 ± 0.01	2.11 × 10^{-4} ± 0.02
	1.6C; 1.6V	−19 ± 0.2	7.02 ± 0.08	0.099 ± 0.003	0.132 ± 0.005	5.9 ± 0.3	6.97 ± 0.02	99.07 ± 0.01	2.62× 10^{-4} ± 0.01
PPy-Nap /Alloy	2C;1.6V	-34 ± 0.3	1.65 ± 0.03	0.023 ± 0.001	0.031 ± 0.001	29.7 ± 0.5	1.35 ± 0.01	99.57± 0.02	6.1× 10^{-5} ± 0.005
	1.6C;1.6V	-39 ± 0.2	5.52 ± 0.04	0.078 ± 0.003	0.104± 0.01	9.8 ± 0.1	5.14 ± 0.02	99.27± 0.005	1.95× 10^{-4} ± 0.02
	2.2C;1.6V	125 ± 0.9	1.35 ± 0.01	0.019 ± 0.001	0.025± 0.002	33.5 ± 0.5	1.35 ± 0.02	99.82± 0.01	1.02× 10^{-5} ± 0.04
	1.6C;1.8V	59 ± 0.4	2.852 ± 0.02	0.040 ± 0.003	0.054± 0.005	19.0 ± 0.2	2.34 ± 0.02	99.62± 0.02	3.61× 10^{-5} ± 0.01
	2C;1mA	-46 ± 0.3	1.26 ± 0.02	0.018 ± 0.001	0.024± 0.001	37.8 ± 0.5	1.25 ± 0.02	99.83± 0.005	5.44× 10^{-5} ± 0.01
	2C;0.5mA	37 ± 0.1	2.96 ± 0.04	0.042 ± 0.002	0.056± 0.002	17.5 ± 0.2	2.72 ± 0.02	99.61± 0.02	4.93× 10^{-5} ± 0.02

EIS confirmed these results. The introduction of Naproxen into the PPy matrix further amplifies the barrier effect. For example, a PPy–NAP film deposited at 1.6 C/1.6 V provides an R_{coat} of approximately 1.4×10^{11} Ω·cm², compared to only 6.4×10^5 Ω·cm² for a similar PPy film. In parallel, R_{ct} increases from ~0.77 kΩ·cm² (1.6 C at 1.6 V) to nearly 15 kΩ·cm² (2.2 C at 1.6 V).

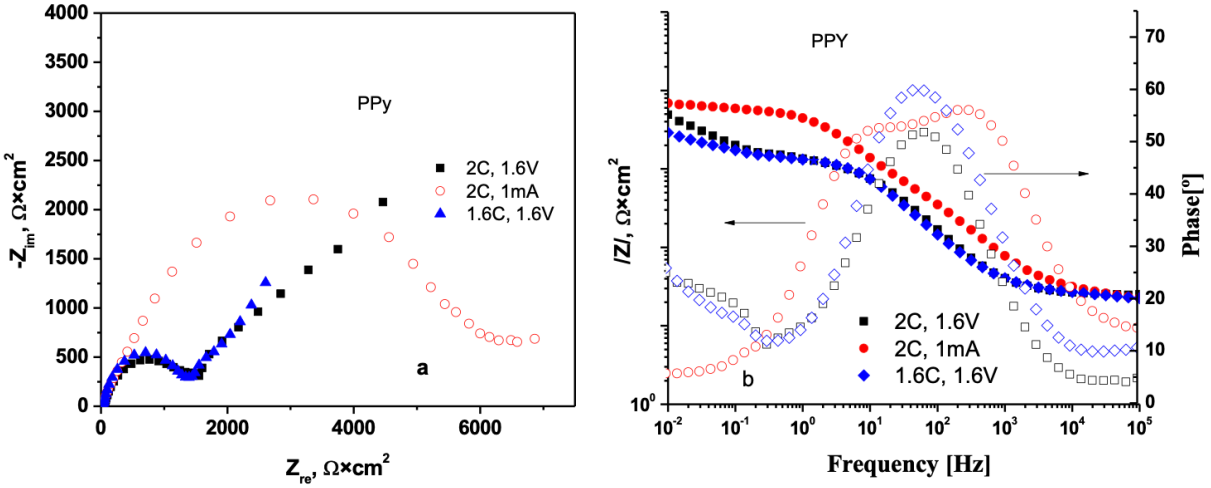

Figure 7.14. Nyquist and Bode plots for Ti-20Zr-5Ta-2Ag+PPy in SBF: potentiostatic depositions at 1.6 V (1.6 C, 2 C) and galvanostatic at 1 mA (2 C)

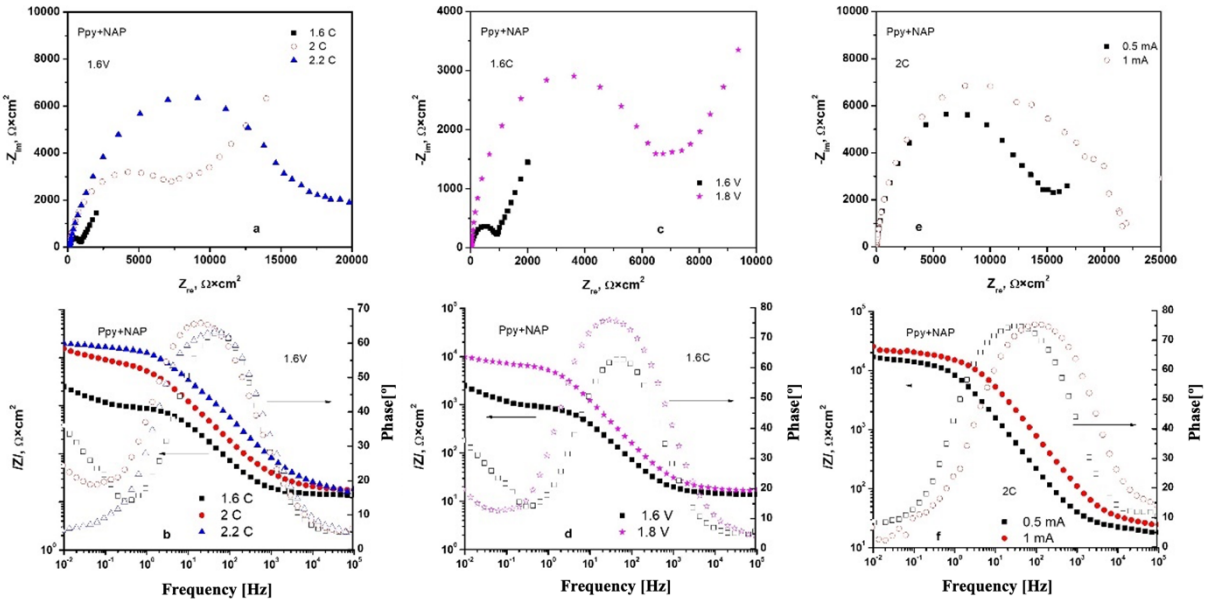

Figure 7.15. Nyquist (top) and Bode (bottom) for PPy–NAP in SBF: potentiostatic depositions at 1.6 V (1.6 C, 2 C, 2.2 C), 1.8 V (1.6 C) and galvanostatic at 0.5 mA and 1 mA (2 C)

SUMMARY

Integrated Approaches to Investigating the Multifunctionality of the Multicomponent Alloy Ti-20Zr-5Ta-2Ag

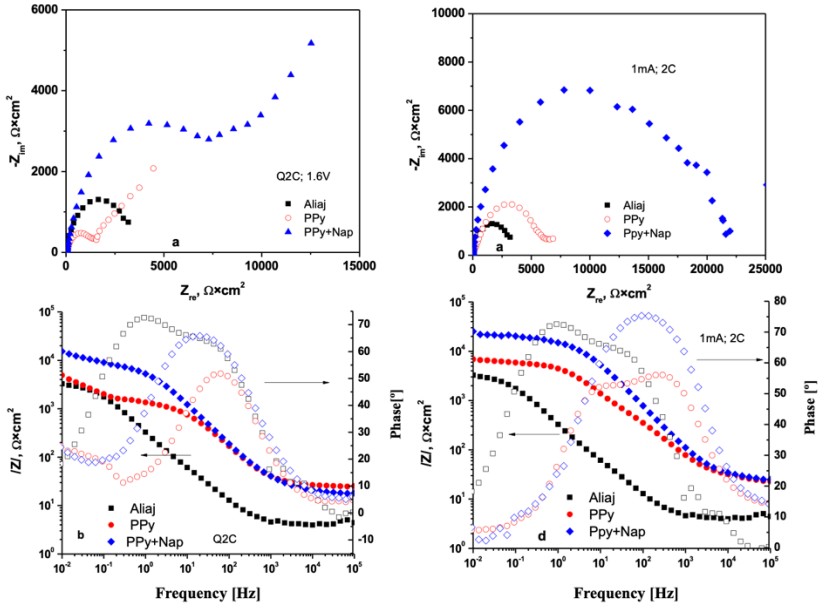

Figure 7.16. Comparative Nyquist (left) and Bode (right) for bare alloy and coated with PPy or PPy–NAP in SBF, prepared in NADES: left panels—chronoamperometric (potentiostatic) deposits; right panels—chronopotentiometric (galvanostatic) deposits

Table 7.2. Fitting parameters of the equivalent circuit obtained by EIS modeling

Material	**Deposition parameters**	**R_s, Ω × cm²**	**R_{ct}, KΩ × cm²**	**CPE_{dl}—T, µF × cm^{-2}**	**CPE_{dl}—P**	**R_{coat}, Ω × cm²**	**CPE_{coat}—T, F × cm^{-2}**	**CPE_{coat}—P**	**Chi-squared (χ2)**
Alloy (bare)	-	4.29	3.39	640	0.84	19.25	0.86× 10^{-3}	0.87	5.1 × 10^{-3}
PPy /Alloy	2C; 1.6V	25.1	1.35	36.6	0.787	4280	1.44× 10^{-3}	0.766	4.1 × 10^{-3}
	2C; 1mA	19.6	6.02	32	0.718	7.43× 10^{9}	3.19× 10^{-3}	0.572	1.7 × 10^{-3}
	1.6C; 1.6V	22.75	1.11	28.2	0.898	6.41× 10^{5}	1.75× 10^{-3}	0.638	1.6× 10^{-4}
PPy+Nap /Alloy	2C;1.6V	23.37	6.42	26.2	0.871	2.59× 10^{4}	0.39× 10^{-3}	0.68	4.8× 10^{-4}
	1.6C;1.6V	13.84	0.77	57.8	0.887	1.43× 10^{11}	2.5× 10^{-3}	0.655	1.1× 10^{-3}
	2.2C;1.6V	24.4	14.98	8.92	0.836	9.3× 10^{9}	4.44× 10^{-4}	0.59	1× 10^{-3}
	1.6C;1.8V	16.37	6.15	17.2	0.947	5.95× 10^{15}	9.66× 10^{-4}	0.548	8× 10^{-4}
	2C;1mA	24.33	11.53	4.16	0.944	11.86× 10^{3}	5.4× 10^{-5}	0.684	6.3× 10^{-3}
	2C;0.5mA	18.68	12.2	16	0.918	10.36×10^{3}	5.75× 10^{-4}	0.562	5.3× 10^{-3}

Release kinetics of Naproxen in SBF at 37 °C were evaluated by UV–Vis at 230 nm: the potentiostatic film shows an initial burst of ~21 % in 3 h and ~94 % release at 192 h, while the galvanostatic film shows ~12 % at 3 h and ~98 % at 192 h (Figure 7.19).

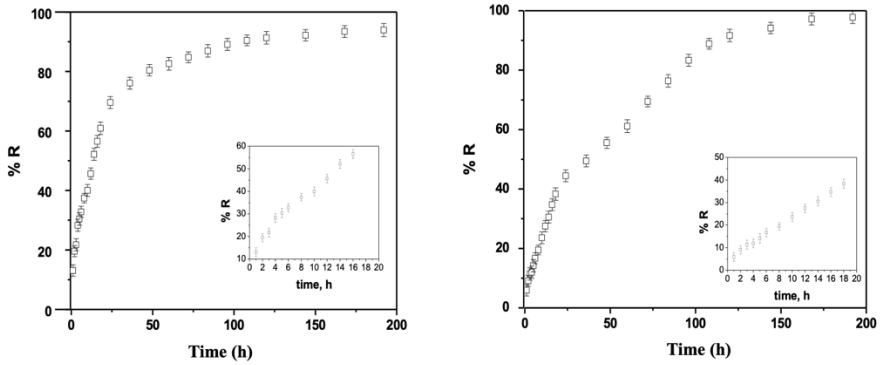

Figure 7.19. Cumulative Naproxen-release profiles in SBF at 37 °C for PPy–NAP (fixed charge = 2 C): (a) potentiostatic deposition (1.6 V); (b) galvanostatic deposition (1 mA)

Empirical model analysis showed that the Peppas–Korsmeyer model best fits the data ($R^2 > 0.99$), with exponent $n \approx 0.505$ (Fickian diffusion) for the potentiostatic film and $n \approx 0.667$ (anomalous non-Fickian diffusion) for the galvanostatic film (Table 7.3).

Table 7.3. Kinetic parameters from empirical model fitting of release data

Deposition mode	**Zero order**		**First order**		**Higuchi**		**Hixson-Crowell**		**Peppas-Korsmeyer**		
	$\%R = k_0 t$		$ln(100 - \%R) = k_1 t$		$\%R = k_2\sqrt{t}$		$\sqrt[3]{100 - \%R} = k_3 t$		$\%R = k_4 \sqrt[n]{t}$		
	R^2	k_0	R^2	k_1	R^2	k_2	R^2	k_3	R^2	k_4	n
Potentiostatic	0,9797	2,62	0,9851	0,0428	0,9885	12,82	0,963	0,053	0,9929	13,29	0,505
Galvanostatic	0,9931	1,88	0,9956	0,024	0,9734	8,51	0,9931	1,65	0,9973	7,73	0,667

In conclusion, by tuning electrochemical parameters (potential, current, charge), synthesis in NADES enables reproducible PPy–NAP films with controlled morphology, superhydrophilicity, enhanced corrosion resistance and sustained Naproxen release. These multifunctional coatings are promising for protective and localized drug-delivery applications.

FINAL CONCLUSIONS

In the present doctoral thesis, the integrated properties and behavior of the multicomponent Ti-20Zr-5Ta-2Ag alloy—a novel material patented in 2019 for biomedical applications—were investigated.

The main objective was to evaluate the multifunctional character of this alloy, which combines favorable mechanical properties (high strength, low elastic modulus), excellent chemical stability in physiological media, and specific biological activity (biocompatibility and antibacterial effect). Accordingly, surface modifications and treatments were optimized to confer a broad spectrum of functional properties, useful in both biomedical applications and aggressive industrial environments. The results confirm that the alloy exhibits complex and versatile behavior, simultaneously delivering mechanical strength, electrochemical stability, biocompatibility, and antibacterial action.

First, surface pre-treatment studies showed that both acid and alkaline etches can be used as complementary tools to calibrate surface topography and energy. Acid etching induced fine roughness, which can enhance adhesion of subsequent functional films. In contrast, alkaline conditioning produced a dense, hydrophilic oxide layer associated with increased microhardness and enhanced chemical inertness. This versatility allows rapid adaptation of the substrate to distinct requirements, from accelerated osteointegration to high abrasion and corrosion resistance.

Second, controlled thermal oxidation between 300 °C and 500 °C generated a uniform oxide layer that doubled microhardness and reduced corrosion current by an order of magnitude without compromising structural integrity. Exceeding 800 °C proved counterproductive, as accelerated grain growth promoted spallation and cracking, diminishing the protective effect of the passive layer. This direct structure–property correlation underscores the necessity of strictly defining the optimal thermal window (300 – 500 °C) as a prerequisite for industrial applications.

On the biofunctionalization front, coatings based on chitosan, bioglass, and graphene oxide outperformed those with ZnO, thanks to GO's dense architecture and barrier properties. The Chi + BG + GO film maintained high anticorrosive protection over 60 days and exhibited pronounced inhibition of *Staphylococcus aureus*, demonstrating its potential to simultaneously reduce electrochemical degradation and microbial colonization.

Concurrently, the electrochemical deposition of polypyrrole–Naproxen films from a natural deep eutectic solvent introduced a multifunctional surface concept that provides an

anticorrosive barrier of up to 10^{15} Ω·cm² and controlled release of the anti-inflammatory drug. The biphasic release profile—an initial burst followed by sustained diffusion over nearly a week—meets clinical demands for immediate post-implant prophylaxis alongside short-term local therapy.

Correlation of these four experimental stages highlights the value of a hierarchical "defense-in-depth" strategy: chemical pre-treatment optimizes roughness and reactivity; thermal oxidation consolidates microhardness and the passive barrier; bioactive coatings impart antibacterial protection; and conductive polymer films add controlled drug-release functionality. Each level contributes additively to corrosion-current reduction and biocompatibility enhancement, yielding performance that significantly exceeds that of any single method.

Original contributions of the thesis include an investigation of how heat treatment influences the structure and properties of the Ti-20Zr-5Ta-2Ag alloy; a comparative analysis of doctor-blade versus MAPLE techniques applied to Chi+BG systems with ZnO versus GO additives, and demonstration of PPy–NAP coatings from natural deep eutectic solvents. Finally, the work maps in detail the relationship between processing parameters, surface structure, and electrochemical/biological performance.

Limitations of the study lie in its predominantly in vitro character. Future stages should include in vivo validation, cyclic-fatigue testing, and advanced modeling of film-tissue interactions at the cellular scale.

In conclusion, this thesis demonstrates that Ti-20Zr-5Ta-2Ag can be transformed, through a carefully sequenced set of treatments, into an advanced materials platform that integrates mechanical strength, electrochemical stability, biocompatibility, and controlled drug release. In doing so, the work not only advances fundamental knowledge but also provides concrete technological premises for the development of next-generation materials.

SELECTIVE BIBLIOGRAPHY

[1] E. V. Vasilescu *et al.*, "Ti-Zr-Ta-Ag Bio-alloy for Orthopedic Implants," RO 132031 B1 / 30.04.2019.
[2] Y. Ma, Y. Li, M. Ou, K. Hou, X. Hao, and M. Wang, "A review on microstructural stability regulation in nickel-based superalloys: synergistic effects of alloying elements and phase stability optimization," *J. Mater. Sci.*, May 2025.
[3] Y. Xu, Y. Li, T. Chen, C. Dong, K. Zhang, and X. Bao, "A short review of medical-grade stainless steel: Corrosion resistance and novel techniques," *J. Mater. Res. Technol.*, vol. 29, pp. 2788–2798, Mar. 2024.
[4] F. Leijon, S. Wachter, Z. Fu, C. Körner, S. Skjervold, and J. Moverare, "A novel rapid alloy development method towards powder bed additive manufacturing, demonstrated for binary Al-Ti, -Zr and -Nb alloys," *Mater. Des.*, vol. 211, p. 110129, 2021.
[5] B. Cantor, I. T. H. Chang, P. Knight, and A. J. B. Vincent, "Microstructural development in equiatomic multicomponent alloys," *Mater. Sci. Eng. A*, vol. 375–377, no. 1-2 SPEC. ISS., pp. 213–218, 2004.
[6] D. B. Miracle and O. N. Senkov, "A critical review of high entropy alloys and related concepts," *Acta Mater.*, vol. 122, pp. 448–511, 2017.
[7] M. Cabrera, Y. Oropesa, J. P. Sanhueza, V. Tuninetti, and A. Oñate, "Multicomponent alloys design and mechanical response: From high entropy alloys to complex concentrated alloys," *Mater. Sci. Eng. R Reports*, vol. 161, no. May, 2024.
[8] B. Liu, W. Yang, G.-H. Cao, and Z. Ren, "Cocktail effect on superconductivity in hexagonal high-entropy alloys," *Phys. Rev. Mater.*, vol. 8, no. 11, p. 114802, Nov. 2024.
[9] A. Yarlapati *et al.*, "Recent advances in additive manufacturing of refractory high entropy alloys (RHEAs): A critical review," *J. Alloy. Metall. Syst.*, vol. 8, no. September, p. 100120, 2024.
[10] C. O. Ujah and D. V. Von Kallon, "Characteristics of phases and processing techniques of high entropy alloys," *Int. J. Light. Mater. Manuf.*, vol. 7, no. 6, pp. 809–824, 2024.
[11] S. Caramarin *et al.*, "Structural Particularities, Prediction, and Synthesis Methods in High-Entropy Alloys," *Appl. Sci.*, vol. 14, no. 17, p. 7576, Aug. 2024.
[12] M. Naseri *et al.*, "Enhancing the mechanical properties of high-entropy alloys through severe plastic deformation: A review," *J. Alloy. Metall. Syst.*, vol. 5, no. November 2023, p. 100054, 2024.
[13] H. Park *et al.*, "Hyperadaptor; Temperature-insensitive tensile properties of Ni-based high-entropy alloy a wide temperature range," *Mater. Res. Lett.*, vol. 13, no. 4, pp. 348–356, Apr. 2025.
[14] F. Madewu, N. Malatji, M. B. Shongwe, T. Marazani, and L. R. Kanyane, "Strength–Ductility Synergy of Lightweight High Entropy Alloys," *Eng. Reports*, vol. 7, no. 3, Mar. 2025.
[15] L. Yang *et al.*, "Al/Cu Enhancement in Marine Anti-Biofouling and Anti-Biocorrosion Performance of High-Entropy Alloys," *Adv. Funct. Mater.*, Apr. 2025.
[16] P. Chakraborty and R. Tewari, "High-entropy alloys for nuclear applications," *J. Mater. Sci.*, vol. 60, no. 3, pp. 1439–1453, Jan. 2025.
[17] S. A. Krishna, N. Noble, N. Radhika, and B. Saleh, "A comprehensive review on advances in high entropy alloys: Fabrication and surface modification methods, properties, applications, and future prospects," *J. Manuf. Process.*, vol. 109, no. December 2023, pp. 583–606, 2024.
[18] B. Cantor, "The thermodynamics of multicomponent high-entropy materials," *J. Mater. Sci.*, vol. 60, no. 3, pp. 1750–1764, Jan. 2025.

[19] V. Verma, C. H. Belcher, D. Apelian, and E. J. Lavernia, "Diffusion in High Entropy Alloy Systems – A Review," *Prog. Mater. Sci.*, vol. 142, p. 101245, Apr. 2024.
[20] W.-L. Hsu, C.-W. Tsai, A.-C. Yeh, and J.-W. Yeh, "Clarifying the four core effects of high-entropy materials," *Nat. Rev. Chem.*, vol. 8, no. 6, pp. 471–485, May 2024.
[21] L. Naveen, P. Umre, P. Chakraborty, M. R. Rahul, S. Samal, and R. Tewari, "Development of single-phase BCC refractory high entropy alloys using machine learning techniques," *Comput. Mater. Sci.*, vol. 238, no. October 2023, p. 112917, 2024.
[22] Y. W. Wang *et al.*, "Ductilization of single-phase refractory high-entropy alloys via activation of edge dislocation," *Acta Mater.*, vol. 284, p. 120614, Jan. 2025.
[23] A. A. Deshmukh and R. Ranganathan, "Recent advances in modelling structure-property correlations in high-entropy alloys," *J. Mater. Sci. Technol.*, vol. 204, pp. 127–151, 2025.
[24] S. Dangwal and K. Edalati, "Developing a single-phase and nanograined refractory high-entropy alloy ZrHfNbTaW with ultrahigh hardness by phase transformation via high-pressure torsion," *J. Alloys Compd.*, vol. 1010, no. December 2024, p. 178274, 2025.
[25] D. Dong *et al.*, "Synergistic strengthening of a TiZrNiAlCu high-entropy alloy by phase transformation and nanophase precipitation under ultrahigh pressure," *Intermetallics*, vol. 178, no. December 2024, p. 108634, 2025.
[26] Y. Zhou *et al.*, "Strategies for optimizing mechanical properties of refractory high entropy alloys induced by solid solution strengthening mechanism," *Mater. Sci. Eng. A*, vol. 923, no. August 2024, p. 147696, 2025.
[27] K. Han, J. Zang, W. He, and J. Chen, "Strength-plasticity trade-off of high-aluminum content AlTiNbV lightweight high-entropy alloy," *Mater. Sci. Eng. A*, vol. 926, no. January, p. 147863, 2025.
[28] M. Ghiasabadi Farahani *et al.*, "Activation of different twinning mechanisms and their contributions to mechanical behavior of a face-centered cubic Co-based high-entropy alloy," *Acta Mater.*, vol. 285, p. 120665, Feb. 2025.
[29] L. Yu, W. Li, W. Lu, H. Feng, and Q. Fang, "Stress gradient versus strain gradient in polycrystalline high entropy alloy revealed by crystal plasticity finite element simulation," *Acta Mech. Sin.*, vol. 41, no. 10, p. 124267, Oct. 2025.
[30] D. Pant and D. S. Aidhy, "Unintuitive alloy strengthening by addition of weaker elements," *npj Comput. Mater.*, vol. 11, no. 1, p. 83, Mar. 2025.
[31] S. Li *et al.*, "Evolution of corrosion mechanism of 3d transition metal high entropy alloys: A review," *J. Mater. Res. Technol.*, vol. 35, no. January, pp. 4142–4163, 2025.
[32] H. Liu *et al.*, "Molecular Dynamics Simulation of the Dynamic Mechanical Behavior of FeNiCrMn High-Entropy Alloy," *Nanomaterials*, vol. 15, no. 8, p. 624, Apr. 2025.
[33] Z. Wang, D. Liu, W. Ji, and M. Li, "Indentation responses and deformation mechanisms of high-entropy alloy coatings on porous Ti6Al4V substrates : Simulations and dimensional analysis," *Mater. Today Commun.*, vol. 44, no. February, p. 112056, 2025.
[34] A. Wei *et al.*, "A new era for applications of multi-principal element alloys in the biomedical field," *Biomater. Adv.*, vol. 172, no. January, p. 214244, Jul. 2025.
[35] A. Rashidy Ahmady, A. Ekhlasi, A. Nouri, M. Haghbin Nazarpak, P. Gong, and A. Solouk, "High entropy alloy coatings for biomedical applications: A review," *Smart Mater. Manuf.*, vol. 1, no. September, p. 100009, 2023.
[36] L. I. N. Tomé, V. Baião, W. da Silva, and C. M. A. Brett, "Deep eutectic solvents for the production and application of new materials," *Appl. Mater. Today*, vol. 10, pp. 30–50, 2018.
[37] Z. Wang, X. Zhao, Y. Chen, C. Wei, and J. Jiang, "A review of designable deep eutectic solvents for green fabrication of advanced functional materials," *RSC Sustain.*, pp. 738–756, 2024.

[38] M. Aslam *et al.*, "Harnessing deep eutectic solvents for advanced corrosion protection: A review," *J. Mol. Liq.*, vol. 422, no. January, p. 126919, 2025.
[39] M. Kaba and H. Cimenoglu, "A study on the durability of oxide coatings fabricated on a refractory high entropy alloy," *Surf. Coatings Technol.*, vol. 505, no. March, p. 132105, 2025.
[40] A. Mazare, G. Totea, C. Burnei, P. Schmuki, I. Demetrescu, and D. Ionita, "Corrosion, antibacterial activity and haemocompatibility of TiO 2 nanotubes as a function of their annealing temperature," *Corros. Sci.*, vol. 103, pp. 215–222, Feb. 2016.
[41] J. E. Berger, A. M. Jorge, G. H. Asato, and V. Roche, "Formation of self-ordered oxide nanotubes layer on the equiatomic TiNbZrHfTa high entropy alloy and bioactivation procedure," *J. Alloys Compd.*, vol. 865, p. 158837, 2021.
[42] T. Xiang, W. Bao, M. Zhao, P. Du, Z. Cai, and G. Xie, "Ultra-high strength TiZrNbTa high entropy alloy substrate coated by coral-like metal oxide nanotubes to enhance biocompatibility," *J. Alloys Compd.*, vol. 923, p. 166408, 2022.
[43] Q. Ahmed, K. Ahmad, A. Aizaz, E. E. S. Massoud, and M. A. U. Rehman, "Controlled biodegradation of AZ31 alloy by chitosan/Fe-doped bioactive glass composite coating deposited via electrophoretic deposition for orthopaedic implants," *Int. J. Biol. Macromol.*, vol. 307, no. P1, p. 141856, 2025.
[44] Z. Mukhtar, A. Dey, and N. Kundan, "Optimized surface engineering of Ti-6Al-4V: Comprehensive coating evaluation for biomedical applications," *Surfaces and Interfaces*, vol. 56, no. January, p. 105735, 2025.
[45] M. Miola *et al.*, "Surface modifications of inert and bioactive glasses with plasma-deposited polymer coatings to impart antiadhesive properties," *Surfaces and Interfaces*, vol. 64, no. March, 2025.
[46] D. A. Ramacharyulu *et al.*, "Recent Advancement in Surface Modification Techniques for Bio-Implants," *Results Eng.*, p. 105192, May 2025.
[47] Q. Du, D. Wei, Y. Wang, B. Li, and Y. Zhou, "Microstructure and surface performance of hydroxyapatite-modified multilayer amorphous coating on Ti-rich TiNbZrSn medium entropy alloy: A comparative study," *Surfaces and Interfaces*, vol. 41, no. 2, p. 103288, 2023.
[48] B. Nasiri-Tabrizi, W. J. Basirun, R. Walvekar, C. H. Yeong, and S. W. Phang, "Exploring the potential of intermetallic alloys as implantable biomaterials: A comprehensive review," *Biomater. Adv.*, vol. 161, no. April, p. 213854, 2024.
[49] J. Dias Corpa Tardelli and A. Cândido dos Reis, "The antibacterial activity and osteoblastic viability of bioactive polymeric coatings on titanium surfaces for dental implants: A systematic review of in vitro studies," *J. Drug Deliv. Sci. Technol.*, vol. 106, no. February, 2025.
[50] R. F. M. dos Santos, P. A. B. Kuroda, G. S. de Almeida, W. F. Zambuzzi, C. R. Grandini, and C. R. M. Afonso, "New MAO coatings on multiprincipal equimassic β TiNbTaZr and TiNbTaZrMo alloys," *Biomed. Eng. Adv.*, vol. 9, no. December 2024, p. 100139, Jun. 2025.
[51] T. S. P. Sousa *et al.*, "Surface aspects of novel Bio-HEAs MAO-treated in a Ca-, P-, and Mg-rich electrolyte," *Appl. Surf. Sci.*, vol. 664, no. May, p. 160227, 2024.
[52] M. Rajabinezhad, A. Bahrami, M. S. Abbasi, and M. R. Karampoor, "A promising multi-component, multi-functional, drug-releasing Cu-doped Fe3O4/bioactive glass/Chitosan coating, applied on stainless steel substrate for biomedical applications," *Int. J. Biol. Macromol.*, vol. 310, no. April, p. 143296, May 2025.
[53] G. Wang *et al.*, "Antibacterial peptides-loaded bioactive materials for the treatment of bone infection," *Colloids Surfaces B Biointerfaces*, vol. 225, no. February, p. 113255,

2023.
[54] M. T. Banizi, M. Khakbiz, S. Shakibania, E. Amiri, and F. Naserian, "Functionalized high entropy alloys with ZIF-8 and LDH nanolayers for next-generation drug eluting medical implants," *J. Alloys Compd.*, vol. 997, no. May, p. 174883, 2024.
[55] H. Wang, Q. Cheng, Z. Chang, K. Wang, X. Gao, and X. Fan, "The Study on Corrosion Resistance of Ti-6Al-4V ELI Alloy with Varying Surface Roughness in Hydrofluoric Acid Solution," *Metals (Basel).*, vol. 14, no. 3, p. 364, Mar. 2024.
[56] I. M. Ribeiro, L. M. Cardoso, T. N. Pansani, A. C. Chagas, C. A. de Souza Costa, and F. G. Basso, "Development of a Bioactive Titanium Surface via Alkalinization and Naringenin Coating for Peri-Implant Repair: In Vitro Study," *Coatings*, vol. 14, no. 10, p. 1303, Oct. 2024.
[57] S. Fernández-Hernández, J. Gil, D. Robles-Cantero, E. Pérez-Pevida, M. Herrero-Climent, and A. Brizuela-Velasco, "Influence of the Sodium Titanate Crystal Size of Biomimetic Dental Implants on Osteoblastic Behavior: An In Vitro Study," *Biomimetics*, vol. 10, no. 1, p. 43, Jan. 2025.
[58] A. J. Antończak, B. Stępak, P. E. Kozioł, and K. M. Abramski, "The influence of process parameters on the laser-induced coloring of titanium," *Appl. Phys. A*, vol. 115, no. 3, pp. 1003–1013, Jun. 2014.
[59] X. Gao, Z. Zhang, L. Liu, and C. Tao, "Microstructure and coloration mechanism of TC11 aerospace titanium alloy ultra-thin thermal oxide films," *J. Mater. Res. Technol.*, vol. 30, pp. 5312–5322, May 2024.
[60] D. Veselinov, R. Yankova, H. Skulev, and I. Rusev, "AN APPROACH FOR THICKNESS ESTIMATION OF ANODIZED TITANIUM OXIDE USING DIGITAL CAMERA," *J. Tech. Univ. Gabrovo*, vol. 69, pp. 37–40, Dec. 2024.
[61] X. Zhang, Z. Zhang, W. Wu, J. Yang, and Q. Yang, "Preparation and characterization of chitosan/Nano-ZnO composite film with antimicrobial activity," *Bioprocess Biosyst. Eng.*, vol. 44, no. 6, pp. 1193–1199, Jun. 2021.
[62] L. Jin *et al.*, "Enhanced mechanical strength and antibacterial properties of Chitosan/Graphene oxide composite fibres," *Cellulose*, vol. 29, no. 7, pp. 3889–3900, May 2022.
[63] O. Długosz, "Natural Deep Eutectic Solvents in the Synthesis of Inorganic Nanoparticles," *Materials (Basel).*, vol. 16, no. 2, p. 627, Jan. 2023.
[64] H. K. Ismail, A. F. Qader, R. A. Omer, H. F. Alesary, H. M. Umran, and A. A. Kareem, "Synthesis of Polypyrrole-Graphene Oxide (PPy/GO) from Deep Eutectic Solvent and Its Characterization for Determination of Metronidazole Pharmaceutical Substance Using Spectrofluorometric Technique," *ChemistrySelect*, vol. 10, no. 8, Feb. 2025.
[65] H. M. Kim, T. Miyazaki, T. Kokubo, and T. Nakamura, "Revised Simulated Body Fluid," *Key Eng. Mater.*, vol. 192–195, pp. 47–50, Sep. 2000.
[66] A. F. Al-Dulaimi, M. M. Al-Kotaji, and F. T. Abachi, "Development of novel paracetamol/naproxen co-crystals with an improvement in naproxen solubility.," *Iraqi J. Pharm. Sci. (P-ISSN 1683 - 3597 E-ISSN 2521 - 3512)*, vol. 31, no. 1, pp. 202–219, Jun. 2022.

SUMMARY

Integrated Approaches to Investigating the Multifunctionality of the Multicomponent Alloy Ti-20Zr-5Ta-2Ag

ANNEX

LIST OF PUBLICATIONS

Published articles

1. **Nartita, R.**; Stoian, A.B.; Ionita, D.; Demetrescu, I. Thermal effects on the mechanical, electrochemical, and surface properties of a Ti20Zr5Ta2Ag alloy for potential industrial and biomedical applications. J. Mater. Res. Technol. **2025**, 35, 7215–7234, doi:10.1016/j.jmrt.2025.02.240. **IF – 6.2, Q1; AIS – 0.884, Q1**
2. Stoian, A.B.; Prodana, M.; **Nartita, R.**; Ionita, D.; Simoiu, M. Antibacterial Properties and Long-Term Corrosion Resistance of Bioactive Coatings Obtained by Matrix-Assisted Pulsed Laser Evaporation on TiZrTaAg. Metals (Basel). **2025**, 15, 253, doi:10.3390/met15030253. **IF – 2.6, Q2; AIS – 0.402, Q2**
3. **Nartita, R.**; Ionita, D.; Demetrescu, I. The performance of high-entropy alloys in aggressive environments. Ann. Acad. Rom. Sci. Ser. Phys. Chem. **2024**, 9, 26–40, doi:10.56082/annalsarsciphyschem.2024.2.26.
4. **Nartita, R.**; Ionita, D.; Demetrescu, I. A Modern Approach to HEAs: From Structure to Properties and Potential Applications. Crystals **2024**, 14, 1–20, doi:10.3390/cryst14050451. **IF – 2.4; Q2; AIS – 0.394, Q2**
5. Demetrescu, I.; **Nartita, R.**; Andrei, M.; Didilescu, A.C.; Cimpean, A.; Ionita, D. Technological Aspects and Performance of High Entropy Alloys with Potential Application in Dental Restorations and Reducing Implant Failure. Appl. Sci. **2023**, 13, 12000, doi:10.3390/app132112000. **IF – 2.5, Q1; AIS – 0.428, Q2**
6. Stoian, A.B.; **Nartita, R.**; Totea, G.; Ionita, D.; Burnei, C. Complex Bioactive Chitosan–Bioglass Coatings on a New Advanced TiTaZrAg Medium–High-Entropy Alloy. Coatings **2023**, 13, 971, doi:10.3390/coatings13050971. **IF – 2.9; Q2, AIS – 0.418, Q3**
7. Golgovici, F.; Tudose, A.E.; Diniasi, D.; **Nartita, R.**; Fulger, M.; Demetrescu, I. Aspects of Applied Chemistry Related to Future Goals of Safety and Efficiency in Materials Development for Nuclear Energy. Molecules **2023**, 28, 874, doi:10.3390/molecules28020874. **IF – 4.2, Q2, AIS – 0.677, Q2**
8. **Nartita, R.**; Andrei, M.; Ionita, D.; Didilescu, A.C.; Demetrescu, I. Can Graphene Oxide Help to Prevent Peri-Implantitis in the Case of Metallic Implants? Coatings **2022**, 12, doi:10.3390/coatings12081202. **IF – 3.4; Q2, AIS – 0.439, Q3**
9. **Nartita, R.**; Ionita, D.; Demetrescu, I.; Enachescu, M. A fresh perspective on medium entropy alloys applications as coating and coating substrate. Ann. Acad. Rom. Sci. Ser. Phys. Chem. **2022**, 7, 34–46, doi:10.56082/annalsarsciphyschem.2022.2.34.
10. **Nartita, R.**; Ionita, D. Influence of Albumin on the corrosion behavior of Ti50Zr alloy. U.P.B. Sci. Bull., Ser. B **2022**, 84.
11. **Nartita, R.**; Ionita, D.; Demetrescu, I. Sustainable Coatings on Metallic Alloys as a Nowadays Challenge. Sustainability **2021**, 13, 10217, doi:10.3390/su131810217. **IF – 3.9, Q2, AIS – 0.516, Q3**

12. **Nartita, R.**; Ionita, D.; Demetrescu, I.; Enachescu, M. Selecting a surface preparation treatment on a medium entropy Ti-Zr-Ta-Ag alloy. Ann. Acad. Rom. Sci. Ser. Phys. Chem. **2021**, 6, 23–31, doi:10.56082/annalsarsciphyschem.2021.2.23.
13. **Nartita, R.**; Ionita, D.; Demetrescu, I. A combined scientometric and critical approach in reviewing TiZr implant alloys and coating performances. Coatings **2021**, 11, 1–28, doi:10.3390/coatings11040392. **IF – 3.2, Q2; AIS – 0.410, Q2**

Cumulative first-author impact factor – 19.1

Total cumulative impact factor – 31.3

Conference participations

1. **Radu NARTIȚĂ**, Florentina GOLGOVICI, Daniela IONIȚĂ, Ioana DEMETRESCU, Improvement of new potential biomaterials and their characterization using techniques such as microscopy, spectroscopy, electrochemistry, chromatography etc., NanoBioMat Conference, Winter Edition **2024**.
2. **Radu NARTIȚĂ**, Andrei Bogdan STOIAN, Daniela IONIȚĂ, Ioana DEMETRESCU, The influence of temperature on the structure and properties of TiZrTaAg high entropy alloy, NanoBioMat Conference, Summer Edition **2024**.
3. **Radu NARTIȚĂ**, Florentina GOLGOVICI, Ioana DEMETRESCU, Aspects of electrodeposition from NADES electrolytes, NanoBioMat Conference, Winter Edition **2023**.
4. **Radu NARTIȚĂ**, Mihai ANDREI, Andreea Cristina DIDILESCU, Daniela IONIȚĂ, Ioana DEMETRESCU, A combined approach in understanding the potential use of high entropy alloys (HEAs) in dentistry, NanoBioMat Conference, Summer Edition **2023**.
5. **Radu NARTIȚĂ**, Manuela FULGER, Ioana DEMETRESCU, Can high entropy alloys be used as structural nuclear materials for future nuclear applications?, NanoBioMat Conference, Winter Edition **2022**.
6. **Radu NARTIȚĂ**, Mihai ANDREI, Daniela IONIȚĂ, Andreea Cristina DIDILESCU, Ioana DEMETRESCU, Composite coatings with graphene oxide for dental and orthopedic implants, NanoBioMat Conference, Summer Edition **2022**.
7. **Radu NARTIȚĂ**, Daniela IONIȚĂ, Ioana DEMETRESCU, Effect of surface preparation treatments on a TiZrTaAg alloy surface, NanoBioMat Conference, Winter Edition **2021**.
8. **Radu NARTIȚĂ**, Daniela IONIȚĂ, Marius ENĂCHESCU, Ioana DEMETRESCU, The influence of proteins on metallic biomaterials, NanoBioMat Conference, Summer Edition **2021**.
9. **Radu NARTIȚĂ**, Daniela IONIȚĂ, Mariana PRODANA, Ioana DEMETRESCU, Aspecte analitice ale spectrometriei de masă cu plasmă cuplată inductiv, NanoBioMat Conference, Winter Edition **2020**.
10. **Radu NARTIȚĂ**, Ioana DEMETRESCU, Raport asupra perspectivelor în identificarea și managementul unor condiții medicale, NanoBioMat Conference, Summer Edition **2020**.